A&A 574, A47 (2015)
DOI: 10.1051/0004-6361/201424873
© ESO 2015

Astronomy & Astrophysics

Imprints of galaxy evolution on H II regions

Memory of the past uncovered by the CALIFA survey*

S. F. Sánchez[1], E. Pérez[2], F. F. Rosales-Ortega[3], D. Miralles-Caballero[4], A. R. López-Sánchez[5,6], J. Iglesias-Páramo[2,7], R. A. Marino[8], L. Sánchez-Menguiano[2,9], R. García-Benito[2], D. Mast[10], M. A. Mendoza[2], P. Papaderos[11], S. Ellis[12,5], L. Galbany[13,14], C. Kehrig[2], A. Monreal-Ibero[15], R. González Delgado[2], M. Mollá[16], B. Ziegler[17], A. de Lorenzo-Cáceres[18], J. Mendez-Abreu[18], J. Bland-Hawthorn[12], S. Bekeraitė[19], M. M. Roth[19], A. Pasquali[20], A. Díaz[4], D. Bomans[21], G. van de Ven[22], L. Wisotzki[19], and The CALIFA collaboration

[1] Instituto de Astronomía, Universidad Nacional Autonóma de Mexico, A.P. 70-264, 04510 México, D.F., Mexico
e-mail: sanchez@iaa.es
[2] Instituto de Astrofísica de Andalucía (CSIC), Glorieta de la Astronomía s/n, Aptdo. 3004, 18080 Granada, Spain
[3] Instituto Nacional de Astrofísica, Óptica y Electrónica, Luis E. Erro 1, 72840 Tonantzintla, Puebla, Mexico
[4] Departamento de Física Teórica, Universidad Autónoma de Madrid, 28049 Madrid, Spain
[5] Australian Astronomical Observatory, PO Box 915, North Ryde, Sydney, NSW 1670, Australia
[6] Department of Physics and Astronomy, Macquarie University Sydney, NSW 2109, Australia
[7] Centro Astronómico Hispano Alemán, Calar Al to, (CSIC-MPG), C/Jesús Durbán Remón 2-2, 04004 Almería, Spain
[8] CEI Campus Moncloa, UCM-UPM, Departamento de Astrofísica y CC. de la Atmósfera, Facultad de CC. Físicas, Universidad Complutense de Madrid, Avda. Complutense s/n, 28040 Madrid, Spain
[9] Dpto. de Física Teórica y del Cosmos, University of Granada, Facultad de Ciencias (Edificio Mecenas), 18071 Granada, Spain
[10] Instituto de Cosmologia, Relatividade e Astrofísica – ICRA, Centro Brasileiro de Pesquisas Físicas, Rua Dr. Xavier Sigaud 150, CEP 22290-180 Rio de Janeiro, RJ, Brazil
[11] Centro de Astrofísica and Faculdade de Ciencias, Universidade do Porto, Rua das Estrelas, 4150-762 Porto, Portugal
[12] Sydney Institute for Astronomy, School of Physics A28, University of Sydney, Sydney, NSW 2006, Australia
[13] Millennium Institute of Astrophysics, Universidad de Chile, Casilla 36-D, Santiago, Chile
[14] Departamento de Astronomía, Universidad de Chile, Casilla 36-D, Santiago, Chile
[15] GEPI, Observatoire de Paris, CNRS UMR 8111, Université Paris Diderot, Place Jules Janssen, 92190 Meudon, France
[16] Departamento de Investigación Básica, CIEMAT, Avda. Complutense 40, 28040 Madrid, Spain
[17] University of Vienna, Türkenschanzstrasse 17, 1180 Vienna, Austria
[18] School of Physics and Astronomy, University of St Andrews, North Haugh, St Andrews, KY16 9SS, UK
[19] Leibniz-Institut für Astrophysik Potsdam (AIP), An der Sternwarte 16, 14482 Potsdam, Germany
[20] Universität Heidelberg, Zentrum für Astronomie, Astronomisches Rechen Institut, Moenchhofstr. 12 – 14, 69120 Heidelberg, Germany
[21] Astronomical Institute of the Ruhr-University Bochum Universitätsstr. 150, 44801 Bochum, Germany
[22] Max-Planck-Institut für Astronomie, 69117 Heidelberg, Germany

Received 28 August 2014 / Accepted 26 September 2014

ABSTRACT

Context. H II regions in galaxies are the sites of star formation, so they are special places for understanding the build-up of stellar mass in the universe. The line ratios of this ionized gas are frequently used to characterize the ionization conditions. In particular, the oxygen abundances are assumed to trace the chemical enrichment of galaxies.

Aims. We explore the connections between the ionization conditions and the properties of the overall underlying stellar population (ionizing or not-ionizing) in H II regions, in order to uncover the actual physical connection between them.

Methods. We use the H II regions catalog from the CALIFA survey, which is the largest in existence with more than 5000 H II regions, to explore their distribution across the classical [O III] λ5007/Hβ vs. [N II] λ6583/Hα diagnostic diagram, and the way it depends on the oxygen abundance, ionization parameter, electron density, and dust attenuation. The location of H II regions within this diagram is compared with predictions from photoionization models. Finally, we explore the dependence of the location within the diagnostic diagram on the properties of the host galaxies, the galactocentric distances, and the properties of the underlying stellar population.

Results. The H II regions with weaker ionization strengths and more metal-rich are located in the bottom righthand area of the diagram. In contrast, those regions with stronger ionization strengths and more metal poor are located in the upper lefthand end of the diagram. Photoionization models per se do not predict these correlations between the parameters and the line ratios. The H II regions located in earlier-type galaxies, closer to the center and formed in older and more metal-rich regions of the galaxies are located in the bottom-right area of the diagram. On the other hand, those regions located in late-type galaxies in the outer regions of the disks and formed on younger and more metal-poor regions lie in the top lefthand area of the diagram. The two explored line ratios show strong correlations with the age and metallicity of the underlying stellar population.

Conclusions. These results indicate that although H II regions are short-lived events, they are affected by the total underlying stellar population. One may say that H II regions keep a memory of the stellar evolution and chemical enrichment that have left an imprint on both the ionizing stellar population and the ionized gas.

Key words. galaxies: abundances – galaxies: star formation – galaxies: evolution – galaxies: ISM

* Appendix A is available in electronic form at http://www.aanda.org

1. Introduction

Classical H II regions are large, low-density clouds of partially ionized gas in which star formation has recently taken place (<15 Myr). The short-lived blue stars forged in these regions emit large amounts of ultraviolet light that ionizes the surrounding gas. They show very different physical scales, from a few parsecs, like the Orion nebula ($D \sim 8$ pc), or even smaller (Anderson 2014), to hundreds of parsecs, such as 30 Doradus ($D \sim 200$ pc), NGC 604 ($D \sim 460$ pc), or NGC 5471 ($D \sim 1$ kpc) as reported by Oey et al. (2003) and García-Benito et al. (2011). These latter ones are the prototypes of the extragalactic giant H II regions found frequently in the disks of spiral galaxies (e.g. Hodge & Kennicutt 1983; Dottori 1987; Dottori & Copetti 1989; Knapen 1998), or starburst and blue compact galaxies (e.g. Kehrig et al. 2008; López-Sánchez & Esteban 2009; Cairós et al. 2012).

Baldwin et al. (1981) first proposed the [O III] λ5007/Hβ versus [N II] λ6583/Hα diagnostic diagram (now known as the BPT diagram) to separate emission-line objects according to the main excitation mechanism: normal H II regions, planetary nebulae, and objects photoionized by a harder radiation field. A hard radiation field can be produced by either a power-law continuum from an active galactic nucleus (AGN), shock excitation, planetary nebulae or even post-AGB stars (e.g. Binette et al. 1994, 2009; Morisset & Georgiev 2009; Flores-Fajardo et al. 2011; Kehrig et al. 2012; Singh et al. 2013; Papaderos et al. 2013). Veilleux & Osterbrock (1987) and Osterbrock (1989) extended and refined this classification scheme, incorporating new diagnostic diagrams. Osterbrock (1989) used theoretical photoionization models to infer the shape of the classification line between star-forming (SF) and AGN galaxies, and they added two new diagnostics diagrams that exploit the [O I]/Hβ versus [S II]/Hα line ratios. Dopita et al. (2000) and Kewley et al. (2001) combined stellar population synthesis and photoionization models to build the first purely theoretical classification scheme for separating pure AGN from galaxies containing star formation, and Kauffmann et al. (2003) used Sloan digital sky survey (SDSS) data to observationally constrain these classifications.

In essence, these models assume that the main factors that control the emission line spectrum are the chemical abundances of the heavy elements in the gas phase of an H II region (oxygen being the most important), the shape of the ionizing radiation spectrum, and the geometrical distribution of gas with respect to the ionizing sources. Generally speaking, all the geometrical factors are subsumed into a single factor, the ionization parameter q (with dimensions cm s^{-1}) or the (dimensionless) ionization parameter $u = q/c$. They also assume a priori that these parameters are independent, and thus these models are presented as grids of oxygen abundance, ionization parameter, and electron densities for a given ionizing population.

Different demarcation lines have been proposed for this diagram. The most popular ones are the Kauffmann et al. (2003) and Kewley et al. (2001) curves. They are usually invoked to distinguish between star-forming regions (below the Kauffmann et al. 2013 curve) and AGNs (above the Kewley et al. 2001 curve). The location between both curves is normally assigned to a mixture of different sources of ionization. Additional demarcation lines have been proposed for the region above the Kewley et al. (2001) curve to distinguish Seyfert and LINERs (e.g., Kewley et al. 2006; Cid Fernandes et al. 2010). More recently the use of 3D diagnostic diagrams has been explored to distinguish the different physical ionization sources in a cleaner way (e.g., Vogt et al. 2014).

There are well known trends in the ionization conditions across the BPT diagram. For example, as the gas-phase chemical abundances are increased, the primary effect on the H II region is to decrease the electron temperature, since there is more cooling per photoionization. This affects the temperature sensitive line ratios, such as [O III] λ4959, λ5007/λ4363, but also many others (e.g., Marino et al. 2013) and, in particular, the two line ratios used in the BPT diagram: [O III] λ5007/Hβ versus [N II] λ6583/Hα. Indeed, early photographic spectra revealed that, in disk galaxies, H II regions located in the outer spiral arms displayed large [O III] λ5007/Hβ ratios, while H II regions located in the inner spiral arms show relatively large [N II] λ6583/Hα ratios (e.g., Sanduleak 1969; Searle 1971). It was soon realized that this is due to the existence of an abundance gradient across the galaxy, connecting the location of H II regions within the BPT diagram with the chemical evolution in disk galaxies for the first time.

Since these early studies, many others have unveiled some aspects of the complex processes at play between the chemical evolution of galaxies and the ionization conditions in H II regions. These studies have been successful in determining important relationships, scaling laws, and systematic patterns: (i) luminosity-metallicity, mass-metallicity, and surface brightness vs. metallicity relations (Lequeux et al. 1979; Skillman 1989; Vila-Costas & Edmunds 1992; Zaritsky et al. 1994; Tremonti et al. 2004); (ii) effective yield vs. luminosity and circular velocity relations (Garnett 2002); (iii) abundance gradients and the effective radius of disks (Diaz 1989); (iv) systematic differences in the gas-phase abundance gradients between normal and barred spirals (Zaritsky et al. 1994; Martin & Roy 1994); (v) characteristic vs. integrated abundances (Moustakas & Kennicutt 2006); (vi) galactocentric abundance gradients (e.g., Bresolin et al. 2009; Yoachim et al. 2010; Rosales-Ortega et al. 2011; Marino et al. 2012; Bresolin et al. 2012), etc.

One problem is that many of these studies, in particular the older ones, present evident selection effects. In most of the cases, the spectroscopic surveys of H II regions rely on previous imaging surveys using narrow-band images (e.g., Martin & Roy 1994). Those images are then processed to provide a catalog of H II regions suitable to being observed using long-slit spectroscopy. In this selection the signal-to-noise ratio of the detected emission line in the narrow-band images plays an important role. Therefore most of these surveys are biased toward high-contrast (equivalent width of emission lines) H II regions located in the outer disks of galaxies. They tend to be focused on late-type spirals (Sc and Sd), which offer the best constrast, thanks to their lower surface-brightness in the continuum. This may have biased our understanding of the properties of H II regions, since in most of the cases the studies were restricted to regions ionized by younger and/or massive stellar clusters. Indeed, Kennicutt et al. (1989) recognized that H II regions in the center of galaxies distinguish themselves spectroscopically from those in the disk by their stronger low-ionization forbidden emission. The nature of this difference was not clear. It may be due to contamination by an extra source of ionization, such as diffuse emission or the presence of an AGN. However, other stellar processes, such as nitrogen enhancement due to the natural aging process of H II regions and the surrounding ISM, can produce the same effect. These early results were confirmed by Ho et al. (1997), who demonstrated that inner star-forming regions may populate the right branch of the BPT diagram at a location above the demarcation line defined later by Kauffmann et al. (2003).

Another bias that may be introduced by classical slit-spectroscopy surveys of H II regions is the aperture effects. As already noticed by Dopita et al. (2014), long-slit observations do not integrate over the whole of an H II region, particularly in the case of observations of nearby galaxies. By picking out the brightest regions of such H II regions, we bias the data toward the high-excitation regions, and the spectrum is not representative of the whole H II region. This is clearly illustrated when the integrated and spatial resolved properties of H II regions are compared (e.g., Sánchez et al. 2007; Relaño et al. 2010; Monreal-Ibero et al. 2011).

The advent of multi-object spectrometers and integral field spectroscopy (IFS) instruments with large fields of view offers us the opportunity to undertake a new generation of emission-line surveys, based on samples of hundreds of H II regions and full two-dimensional (2D) coverage of the disks of nearby spiral galaxies (e.g., Rosales-Ortega et al. 2010; Sánchez et al. 2012a, 2014). Large catalogs of H II regions have been produced, with thousands of objects, over statistical samples of galaxies covering a wide range of morphological types (Sánchez et al. 2012b, 2013). These catalogs have led to the discovery of: (i) a clear correlation between the oxygen abundance of individual H II regions and the stellar mass densities of the underlying stellar population (Rosales-Ortega et al. 2012; Sánchez et al. 2013); (ii) a radial gradient of different ionization conditions (Sánchez et al. 2012b); and (iii) the existence of a common abundance gradient in all disk-dominated galaxies (Sánchez et al. 2014). Interestingly, these results confirmed the previous ones presented by Kennicutt et al. (1989) and Ho et al. (1997), regarding the presence of H II regions above the demarcation line defined by Kauffmann et al. (2003). Those H II regions are not restricted to the central regions and can be found at any galactocentric distance, even at more than 2 r_e, which excludes or minimizes a possible contamination by a central source of ionization. A more plausible explanation is that we are observing more aged H II regions, as indicated before.

All these relations point toward a connection between the ionization conditions in H II regions and the properties of the underlying stellar population, hence, the overall evolution of the host galaxies. This connection is not taken into account by photoionization models. Evolutionary processes of the ionizing cluster (e.g., Dopita et al. 2006a) and/or constraints imposed by the evolution of the host galaxies (e.g., Dopita et al. 2006b) are required to explain these relations.

In the current study we explore the distribution of H II regions across the BPT diagram to try to understand the nature of this connection. To do so, we have used the largest catalog of H II regions with the spectroscopic information currently available. This catalog was extracted from the CALIFA dataset (Sánchez et al. 2012a), and it comprises more than 5000 H II regions (Sánchez et al. 2014). The structure of this article is as follows: Sect. 2 presents the sample of galaxies and H II regions used throughout this study. Section 3 summarizes the analysis of the data. Section 3.1 comprises the comparison between the distribution across the BPT diagram with photoionization models. In Sect. 3.2 we explore how the parameters that define the ionization conditions actually change across the BPT diagram. Sections 3.3 and 3.4 explore the change in the distribution of H II regions as a function of the morphology of the host galaxy and their galactocentric distance. Finally, Sect. 3.5 explores the dependency of the location within the BPT diagram with the properties of the underlying stellar population. Section 4 discusses the results of the analysis, and the conclusions are summarized in Sect. 5.

2. Sample of galaxies and dataset

The galaxies were selected from the CALIFA observed sample. Since CALIFA is an ongoing survey whose observations are scheduled on a monthly basis (i.e., dark nights), the list of objects increases regularly. The current results are based on the 306 galaxies observed before May 2013. Their main characteristics have already been described in Sánchez et al. (2014).

The details of the survey, sample, observational strategy, and reduction are explained in Sánchez et al. (2012a). All galaxies were observed using PMAS (Roth et al. 2005) in the PPAK configuration (Kelz et al. 2006), covering a hexagonal field of view (FoV) of $74'' \times 64''$, which is sufficient to map the full optical extent of the galaxies up to two to three disk effective radii. This is possible because of the diameter selection of the sample (Walcher et al. 2014). The observing strategy guarantees complete coverage of the FoV, with a final spatial resolution of $FWHM \sim 3''$, corresponding to ~1 kpc at the average redshift of the survey. The sampled wavelength range and spectroscopic resolution (3745−7500 Å, $\lambda/\Delta\lambda \sim 850$, for the low-resolution setup) are more than sufficient to explore the most prominent ionized gas emission lines from [O II] λ3727 to [S II] λ6731 at the redshift of our targets, on one hand, and to deblend and subtract the underlying stellar population, on the other (e.g., Sánchez et al. 2012a; Kehrig et al. 2012; Cid Fernandes et al. 2013, 2014). The dataset was reduced using version 1.3c of the CALIFA pipeline, whose modifications with respect to the one presented in Sánchez et al. (2012a) are described in detail in Husemann et al. (2013). In summary, the data fulfill the predicted quality-control requirements with a spectrophotometric accuracy that is better than 15% everywhere within the wavelength range, both absolute and relative with a depth that allows us to detect emission lines in individual H II regions as faint as $\sim 10^{-17}$ erg s^{-1} cm^{-2}, and with a signal-to-noise ratio of $S/N \sim 3-5$. For the emission lines considered in the current study, the S/N is well above this limit, and the measurement errors are negligible in most of the cases. In any case, they have been propagated and included in the final error budget.

The final product of the data reduction is a regular-grid datacube, with x and y coordinates that indicate the right ascension and declination of the target, and z a common step in wavelength. The CALIFA pipeline also provides the propagated error cube, a proper mask cube of bad pixels, and a prescription of how to handle the errors when performing spatial binning (due to covariance between adjacent pixels after image reconstruction). These datacubes, together with the ancillary data described in Walcher et al. (2014), are the basic starting points of our analysis.

2.1. H II detection and extraction

The segregation of H II regions and the extraction of the corresponding spectra is performed using a semi-automatic procedure named H IIEXPLORER[1]. The procedure is based on some basic assumptions: (a) H II regions are peaky and isolated structures with a strong ionized gas emission, which is significantly above the stellar continuum emission and the average ionized gas emission across the galaxy. This is particularly true for Hα because (b) H II regions have a typical physical size of about a hundred or a few hundred parsec (e.g., González Delgado & Perez 1997; Lopez et al. 2011; Oey et al. 2003), which corresponds to a typical projected size of a few arcsec at the distance of the galaxies.

[1] http://www.caha.es/sanchez/HII_explorer/

These basic assumptions are based on the fact that most of the Hα luminosity observed in spiral and irregular galaxies is a direct tracer of the ionization of the interstellar medium (ISM) by the ultraviolet (UV) radiation produced by young high-mass OB stars. Since only high-mass, short-lived stars contribute significantly to the integrated ionizing flux, this luminosity is a direct tracer of the current star-formation rate (SFR), independent of the previous star-formation history. Therefore, clumpy structures detected in the Hα intensity maps are most probably associated with classical H II regions (i.e., those regions for which the oxygen abundances have been calibrated).

The details of H IIEXPLORER are given in Sánchez et al. (2012b) and Rosales-Ortega et al. (2012). In summary we create a narrow-band image centered on the wavelength of Hα at the redshift of the object. Then we run H IIEXPLORER to detect and extract the spectra of each individual H II region, adopting the parameters presented in Sánchez et al. (2014). The algorithm starts looking for the brightest pixel in the map. Then, the code aggregates the adjacent pixels until all pixels with flux greater than 10% of the peak flux of the region and within 500 pc or 3.5 spaxels from the center have been accumulated. The distance limit takes the typical size of H II regions of a few hundreds of parsecs into account (e.g., González Delgado & Perez 1997; Lopez et al. 2011). Then, the selected region is masked and the code keeps iterating until no peak with flux exceeding the median Hα emission flux of the galaxy is left. Mast et al. (2014) studied the loss of resolution in IFS using nearby galaxies observed by PINGS (Rosales-Ortega et al. 2010). Some of these galaxies were simulated at higher redshifts to match the characteristics and resolution of the galaxies observed by the CALIFA survey. Regarding the H II region selection, the authors conclude that at $z \sim 0.02$, the H II clumps can contain on average from 1 to 6 of the H II regions obtained from the original data at $z \sim 0.001$. Another caveat is that this procedure tends to select regions with similar sizes, although real H II regions actually have different sizes. However, the actual adopted size is close to the FWHM of the CALIFA data for the version of the data reduction we used (Husemann et al. 2013).

Then, for each individual extracted spectrum we modelled the stellar continuum using FIT3D[2], a fitting package described in Sánchez et al. (2006, 2011). A simple SSP template grid with 12 individual populations was adopted. It comprises four stellar ages (0.09, 0.45, 1.00, and 17.78 Gyr), two young and two old ones, and three metallicities (0.0004, 0.019, and 0.03, that is, subsolar, solar, or supersolar, respectively). The models were extracted from the SSP template library provided by the MILES project (Vazdekis et al. 2010; Falcón-Barroso et al. 2011). The use of different stellar ages and metallicities or a larger set of templates does not qualitatively affect the derived quantities that describe the stellar populations. Indeed, we compared two of these parameters (luminosity-weighted age and metallicity), derived using this simple template and the more elaborate one described in Cid Fernandes et al. (2013, 2014), and we found a agreement within ~0.25 dex in both parameters.

After subtracting the underlying stellar population, the flux intensity of the strong emission lines was extracted for each gas-pure spectrum by fitting a single Gaussian model to each line, resulting in a catalog of the emission-line properties (Sánchez et al. 2012b). Finally, the H II regions were selected from this final catalog based on the properties of the underlying stellar continuum. It was required that they present a young stellar population, compatible with the observed equivalent width of Hα (Sánchez et al. 2014).

The final catalog comprises the strongest emission line and emission line ratios from [O II] λ3727 to [S II] λ6731 for 5229 H II regions, together with their equivalent widths and the luminosity-weighted ages and metallicities of the underlying stellar population. So far, this is the largest catalog of H II regions and aggregations with spectroscopic information. It is also one of the few catalogs derived for a statistically well-defined sample of galaxies representative of the entire population of galaxies in the Local Universe (Walcher et al. 2014).

3. Analysis and results

The main goal of this study is to understand how the ionization conditions in H II regions are related to the properties of the galaxies and if there is a connection between the ionization conditions and the overall evolution and chemical enrichment of the stellar populations. To do so we use the catalog of emission-line fluxes and ratios and the corresponding properties of the stellar populations of the H II regions sample described before (Sánchez et al. 2014).

3.1. Distribution of H II regions across the BPT diagram

Figure 1 shows the distribution of our sample of H II regions across the BPT diagram compared with different photoionization models. The Kauffmann et al. (2003) and Kewley et al. (2001) demarcation lines have been included as general references. The two panels in the top include the expected location based on the MAPPINGS-III photoionization models (Allen et al. 2008), when adopting two different ionizing populations (Kewley et al. 2001). The top lefthand panel shows the grid that corresponds to an instantaneous zero-age starburst model based on the PEGASE spectral energy distribution (Kewley et al. 2001; Dopita et al. 2000). Each red solid line corresponds to a different metallicity, which is indicated with the corresponding label (ranging from 0.2 to 2.0 solar abundances), and each blue solid line corresponds to a different ionization parameter of the radiation field (ranging from $\log(u) = -3.7$, at the bottom, to $\log(u) = -2$, at the top). The top righthand panel shows a similar plot, the only difference being that here we assumed a continous starburst model 4 Myr since its ignition. In all cases an average electron density of $n_e = 350$ cm^{-3} is assumed.

As expected, most of the H II regions are located below the envelope defined by the instantaneous starburst photoinization models, which was proposed by Dopita et al. (2000) as a demarcation line to define the regions that are clearly ionized by star-formation. This line is very similar to the empirical one defined by Kauffmann et al. (2003), and the theoretical one defined by Stasińska et al. (2006). We adopted the Kauffmann et al. (2003) one here, but using any of the three will produce similar results. However, there is a non-negligible fraction of ~14% of H II regions located between this envelope and the one defined by a model with continuous star formation, as we already noted in Sánchez et al. (2013, 2014). Kewley et al. (2001) noted that starburst galaxies are mainly located in this region. They considered these galaxies to have experienced ongoing star formation over at least several Myr, and this prolonged star-formation activity is reflected in the BPT diagrams. A similar interpretation can be applied to the H II regions above the Dopita et al. (2000) and/or Kauffmann et al. (2003) demarcation lines.

In both a single burst or continuous star formation, the distribution of H II regions across the BPT diagram does not cover

[2] http://www.caha.es/sanchez/FIT3D/

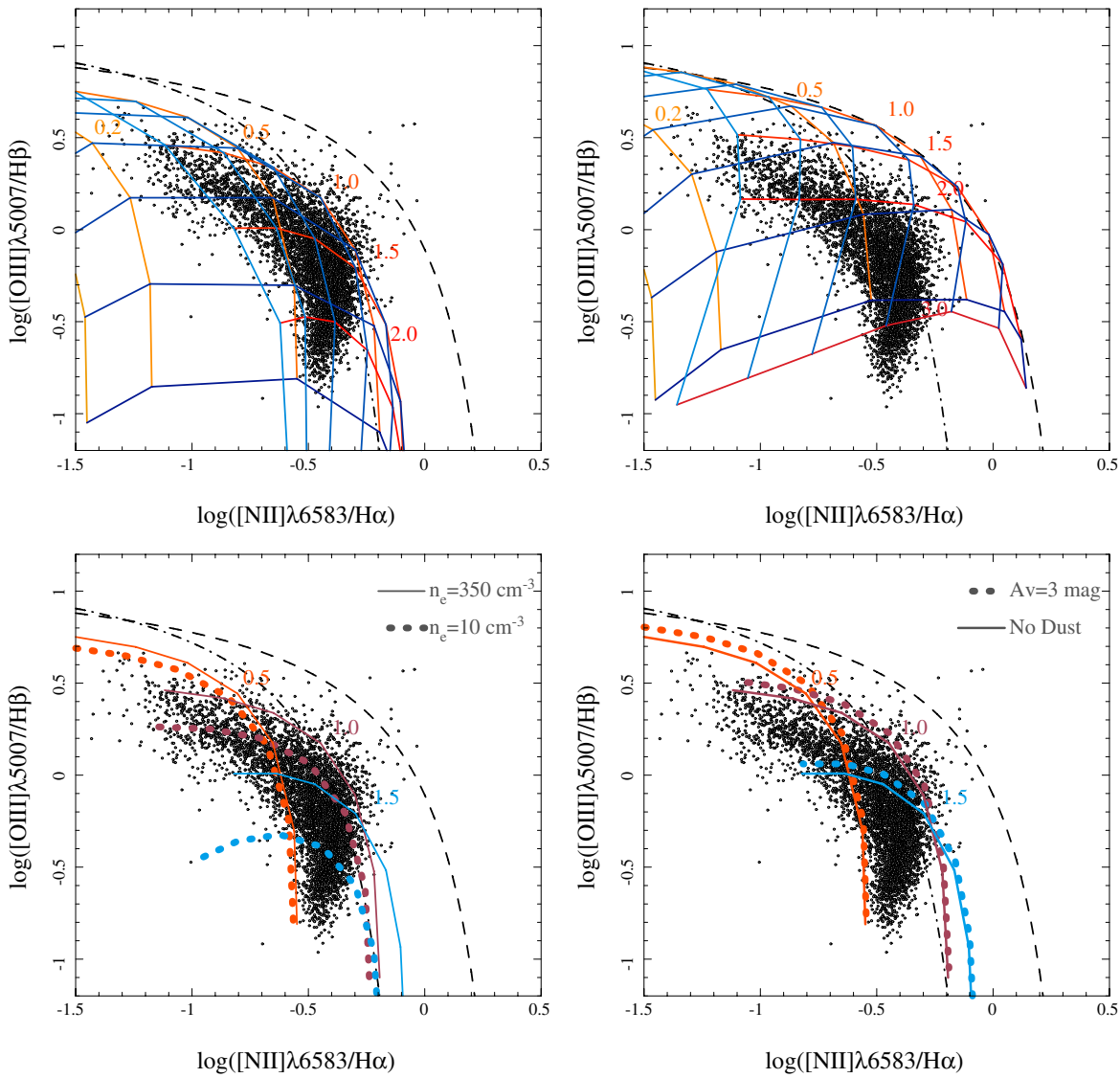

Fig. 1. *Top left panel*: distribution of the [O III] λ5007/Hβ vs. [N II] λ6583/Hα line ratios for the ~5000 H II ionized regions included in our sample. The colored solid lines represent the expected line ratios derived from the MAPPINGS-III ionization models, based on an instantaneous zero-age starburst model based on the PEGASE spectral energy distribution (Kewley et al. 2001; Dopita et al. 2000), and a fixed electron density of 350 cm^{-3}. Each orange-to-red solid line corresponds to a different metallicity, which is indicated with the corresponding label and color (ranging from 0.2 to 2.0 solar metallicities), and each blue-to-cyan solid-line corresponds to a different ionization parameter of the radiation field (ranging from $\log(u) = -3.7$, for the dark blue, to $\log(u) = -2$, at the cyan blue). *Top right panel*: similar plot, with the only difference being that now the colored solid lines represent the expected line ratios for a continuous starburst model 4 Myr since its ignition. *Bottom left panel*: similar plot, with the only difference being in this case that the colored solid lines and the dotted lines correspond to the expected line ratios for a photoionization model based on an instantaneous zero-age starburst, with a constant metallicity (indicated with a label and represented with a fixed color), but for two different electron densities (10 cm^{-3}, for the dotted line, and 350 cm^{-3}, solid one). *Bottom-right panel*: similar plot, with the only difference being that in this case the colored solid lines and the dotted lines correspond to the expected line ratios for a photoionization model based on an instantaneous zero-age starburst, with constant metallicity and a fixed electron density shown in *top left panel*, but for two different dust attenuations (no dust, for the solid-line, and $A_V = 3$ mag for the dotted one). In all the panels, the dot-dashed and dashed line represent the Kauffmann et al. (2003) and Kewley et al. (2001) demarcation curves, respectively. They are usually invoked to distinguish between classical star-forming objects (below the dashed dotted line), and AGN powered sources (above the dashed line). Regions between both lines are considered intermediate ones.

the entire parameter space forseen by the considered photoionization models. Thus, real H II regions cover a smaller parameter space than is predicted by the models. On the other hand, there is a degeneracy in the combination of ionization conditions that predict a certain location in the diagram (abundance and ionization strength in this particular grid). Therefore, the location of a particular H II could be explained by different ionization conditions. For example, the curve described for a fixed solar abundance present values within the BPT diagram that range from $(-1, 0.5)$ in the upper lefthand corner to $(-0.2, -1)$, in the bottom righthand corner. Indeed, it almost describes an envelope of the distribution of H II regions across the BPT diagram (Fig. 1). Only when fixing one of the two parameters involved in the grid is it possible to derive a trend with the other parameter across the BPT diagram. Both results have two direct consequences: (i) it is not possible to derive which ioniziation conditions are associated with a particular H II region only based on their location in the BPT diagram; and (ii) there are ionization conditions that

are discarded for reasons that cannot be predicted based only on photoionization models. This result is well known and has limited our ability to recover the ionization conditions of H II regions for decades (e.g., Pérez-Montero 2014).

We explore how the variation in other parameters affects the line ratios predicted by photoionization models. The bottom lefthand panel of Fig. 1 illustrates the change in the location across the BPT diagram when different electron densities are assumed. We show the same grid of photoinization models presented in the top lefthand panel, but assuming two different electron densities (n_e = 10 and 350 cm^{-3}). In general the photoionization models predict that higher density regions of similar abundances and ionization strengths should be located at higher values of [O III]/Hβ for very similar values of [N II]/Hα. Therefore, the regions located in the top righthand envelope of the distribution should be the densest ones.

Finally, we explore the variation in the line ratios when dust attenuation is taken into account. The bottom righthand panel of Fig. 1 shows the same grid of photoionization models presented in the top lefthand panel, but assuming two different dust attenuations (A_V = 0 and 3.5 mag). The effects of the dust attenuation over the line ratios were simulated adopting the Cardelli et al. (1989) extinction law, with a specific dust attenuation of R_V = 3.1. The BPT diagram is designed to be less affected by dust attenuation than other frequently used ones (e.g., Veilleux et al. 1995), since it involves emission lines at very similar wavelengths for each ratio. Thus, even in the case of very large dust attenuations, the differences are very small. Therefore, no trend is expected with the dust attenuation in the distribution of H II regions across the BPT diagram.

3.2. Empirical estimation of the ionization parameters

We have seen in the previous section that the location in the BPT diagram for a classical H II region ionized by young stars of a certain age is defined well by three main parameters: (a) the ionization parameter or fraction of Lyman continuum photons with respect to total amount of gas; (b) the metallicity or chemical abundance of the ionized gas; and (c) the electron density of the gas. In addition, we have seen that the location should have no dependency on the dust attenuation (for this particular diagram). However, the trends of the two first parameters across the BPT diagram are not defined well based on photoinization models. We investigate here how the oxygen abundance, ionization strength, electron density, and dust attenuation actually change across the BPT diagram, based on empirical estimations of these parameters.

The oxygen abundances were derived using the counterpart method described by Pilyugin et al. (2012). This method uses the dust-corrected emission line ratios of a set of strong emission lines including [O II]/Hβ, [O III]/Hβ, [N II]/Hβ, and [S II]/Hβ and compares the input values with a grid of line ratios of H II regions with known abundances derived using the direct method (i.e., based on direct estimations of the electron temperature). This calibrator attempts to improve the previously analytical method proposed in Pilyugin et al. (2010). The values derived using this method were cross-checked with the ones provided using the O3N2 calibrator (Alloin et al. 1979; Pettini & Pagel 2004; Stasińska et al. 2006),

$$\mathrm{O3N2} = \log\left[\frac{I([\mathrm{O\,III}]\,\lambda5007)/I(\mathrm{H}\beta)}{I([\mathrm{N\,II}]\,\lambda6584)/I(\mathrm{H}\alpha)}\right] \quad (1)$$

using the recently updated calibration presented by Marino et al. (2013), which improves the abundance estimation by including many more H II regions than previous calibrations using this parameter (e.g., Pettini & Pagel 2004), in particular in the range of higher metallicities. The advantage of this method is that it depends on strong, well-deblended emission lines, and in particular does not depend on [O II] λ3727, a line that may be affected by vignetting (Sánchez et al. 2012a), any inaccuracy in flux calibration in the blue end of the covered spectral range (Husemann et al. 2013), and uncertainties related to the derivation of the dust attenuation. The values for oxygen abundances match one another within a standard deviation of ~0.07 dex, a value near the expected errors of the individual measurements (Sánchez et al. 2013) and the accuracy of the calibrators (Marino et al. 2013).

For the ionization parameter, u, we adopted two different calibrators described by Díaz et al. (2000), based on [S II] λ6717,6731/Hβ, and [O II] λ3727/Hβ, which requires previous knowledge of the oxygen abundance, and a third one described by Dors et al. (2011), which depends on the [O II]/[O III] line ratio. This last is a recalibration of the classical one proposed by Díaz et al. (2000). We cross-checked the values obtained by the different methods, and they seem to agree within the errors, although [S II]/Hβ yields slightly higher values than the other two. We adopted the mean value of the three as our estimation of the ionization parameter. Recent results indicate that other line ratios, like [O III]/[S II], can be used as good tracers of the ionization parameter (Dopita et al. 2013). However, there is no published calibrator corresponding to this ratio to our knowledge, and therefore we could not compare the results in an independent way. As a final sanity check, we cross-checked that the derived values follow the described relation between this parameter and the equivalent width of Hβ (Diaz 1989).

The electron density, n_e, was derived based on the line ratio of the [S II] doublet (e.g., Osterbrock 1989), by solving the equation,

$$\frac{I([\mathrm{S\,II}]\,\lambda6717)}{I([\mathrm{S\,II}]\,\lambda6731)} = 1.49\frac{1+3.77x}{1+12.8x} \quad (2)$$

where x is the density parameter, defined as $x = 10^{-4}n_e t^{-1/2}$ and t is the electron temperature in units of 10^4 K (McCall et al. 1985). For this calculation we assumed a typical electron temperature of $T = 10^4$ K, which is an average value that corresponds to the expected conditions in H II regions (Osterbrock 1989). This equation reflects that the [S II] doublet ratio is sensitive to changes in the electron density only for a limited range of values. For high and low values, it becomes asymptotic, and the actual derived value has to be treated with care and should not be used for quantitative statements. However, the value will still be valid for the purposes of this study, allowing us to understand the general trends across the BPT diagram with the electron density.

Finally, the dust attenuation, A_V, was derived based on the Hα/Hβ Balmer line ratio. The extinction law by Cardelli et al. (1989) was assumed, with a specific dust attenuation of R_V = 3.1, and the theoretical value for the unobscured line ratio for case B recombination of Hα/Hβ = 2.86, for T_e = 10 000 K and n_e = 100 cm^{-3} (Osterbrock 1989). For this study we have assumed that the intrinsic Hα/Hβ line ratio does not vary significantly, although it is known that it presents a dependence with the electron density and the temperature (e.g., Sánchez et al. 2005).

3.2.1. Distribution across the BPT diagram

The top lefthand panel of Fig. 2 shows the distribution of H II regions across the BPT diagram, with a color code representing the

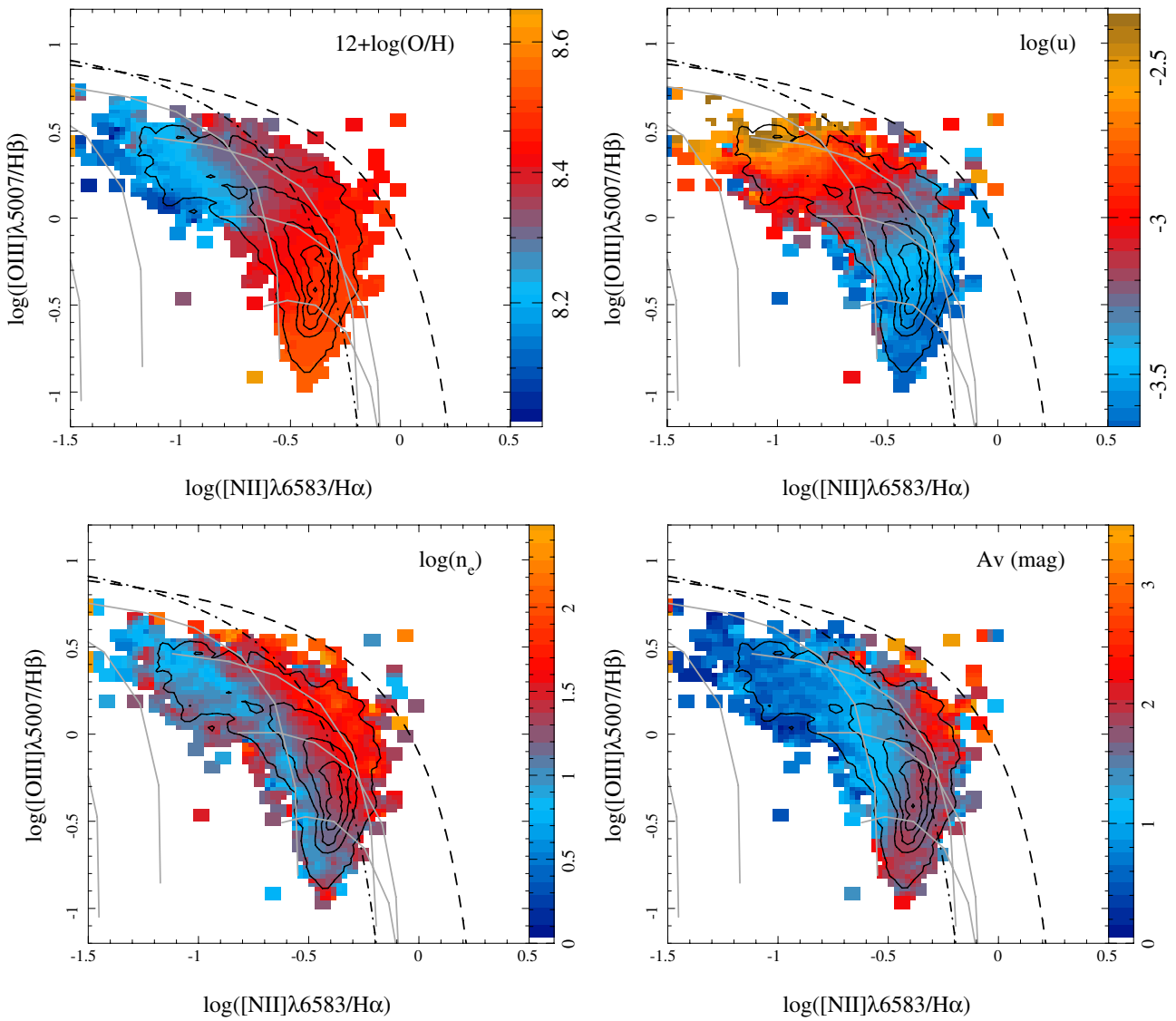

Fig. 2. [O III] λ5007/Hβ vs. [N II] λ6583/Hα diagnostic diagram for the ~5000 H II regions included in our sample. The contours show the density distribution of these regions within the diagram plane, with the outermost contour enclosing 95% of the regions and each consecutive one enclosing 20% fewer regions. In each panel the color indicates the average value at the corresponding location in the diagram for one of the four parameters described in the text: *top left panel*: oxygen abundance; *top-right panel*: ionization parameter; *bottom left panel*: electron density; and *bottom right panel*: dust attenuation. In all panels, the dot-dashed and dashed lines represent, respectively, the demarcation curves described in Fig.1, and the gray solid lines represent the expected line ratios derived from the photoionization models shown in Fig. 1, where each line corresponds to a different stellar metallicity (orange-to-red solid lines in Fig. 1).

oxygen abundance in each region. The more metal-poor H II regions are located in the upper lefthand corner of the diagram, and the more metal-rich ones are located toward the lower righthand corner. None of these trends can be explained only by the expected values derived from photoionization models, as seen in the previous section. The opposite trend is found for the ionization parameter. The top lefthand panel of Fig. 2 shows the same distribution with a color code representing the value of the ionization parameter in each region. There is a clear trend across the diagram. The H II regions with the largest ionization parameter are located in the upper lefthand corner of the diagram, and those with the lowest values of this parameter are located toward the lower righthand corner.

The bottom lefthand panel of Fig. 2 shows the distribution of H II regions across the BPT diagram with a color code representing the electron density. The denser regions are located toward the upper righthand envelope of the distribution, as expected from the comparison with photoionization models presented in the previous section. Regions with higher electron density are expected in areas of the galaxy that have suffered from an overpressure, in particular in the leading front of a density wave generated by spiral arms or toward the central regions of the galaxies. We investigate that possibility in the next sections.

Finally, we explore the relation between the distribution of H II regions across the BPT diagram and the amount of dust attenuation. The bottom righthand panel of Fig. 2 shows the same distribution as shown in previous panels with a color code representing the dust attenuation derived from the Balmer decrement. There is a clear trend that is not taken into account by photoionization models, because by construction, the location within the BPT diagram ought to be independent of dust attenuation. Regions with lower dust attenuation are located in the upper lefthand region of the diagram, with A_V increasing toward the lower righthand and then increasing again at the upper righthand

end of the diagram. Indeed, the regions with the largest dust attenuation are those located in the so-called intermediate area, defined as the region between the Kauffmann et al. (2003) and Kewley et al. (2001) curves.

We should note here that the derived parameters may present crossdependences owing to the adopted formulae or calibration to derive them. We tried to minimize or quantify those possible dependences to exclude possible induced trends. For the oxygen abundance, we adopted the counterpart method since it uses all the strong emission lines in the considered wavelength range, and not only those involved in the H II diagram (like O3N2 or N2 calibrators Marino et al. 2013). We repeated the analysis using other abundance indicators, such as R23 or N2S2, without significant differences in the described trends. The ionization parameter was derived using different calibrators, but only one of them is purely empirical (the one based on the [O II]/[O III] line ratio). The other two calibrators involve deprojections of photoionization models that try to remove the degenerancy in the derivation of the oxygen abundance and the ionization-parameter. We consider that this approach minimizes the possible dependencies between those two parameters induced by the adopted estimators are minimized.

The derivation of the electron density is based on a formula derived from the basic principles of the quantum physic (Eq. (2)). This equation provides an electron density that depends on the electron temperature. We fixed this second parameter, and therefore we may have induced a possible secondary correlation with any other parameter that depends on the temperature, such as the oxygen abundance or the ionization strength. However, the largest possible bias introduced by fixing the electron temperature in the derivation of n_e is a factor 2−3. This cannot explain the range of derived electron densities two orders of magnitudes or their pattern in the BPT diagram.

Finally, in deriving of the dust attenuation, we assumed a fixed value for the intrinsic Balmer line ratios: $H\alpha/H\beta = 2.86$. However, it is well known that this line ratio depends on the ionization conditions within the nebulae, and it can range between 2.7 and 3.1 for usual H II regions (e.g., Osterbrock 1989). The possible effect of taking this detail into account in the derivation of the dust attenuation has been explored by previous studies and in general it has been found that the differences in the derived dust attenuations is very small (e.g., Sánchez et al. 2007). In general, the possible trends of the derived A_V with the electron temperature and electron density are weaker than the observational errors of the considered line ratio or other effects (such as assuming an uncorrect dust attenuation law or a Milky-Way specific dust attenuation). In summary, we consider that the described trends are genuine and not induced by possible correlations implicit in the estimations used to derive each parameter.

The described trends across the BPT diagram of the parameters that define the ionization conditions imply that there are correlations between those parameters that cannot be explained based purely on photoionization models. Figure 3 shows the distribution of oxygen abundance along the ionization parameter. As expected, there is a clear correlation. Those regions with higher oxygen abundance have the lowest ionization strengths, and those regions with the lowest oxygen abundances have the highest ionization strengths. This is a well known relation, described for the first time by Dopita & Evans (1986), using strong-line indicators of both parameters. More recently, Pérez-Montero (2014) has explored this relation based on a collection of H II regions with abundances derived using the direct method, i.e., based on the electron tempeture, described in Marino et al. (2013). The results of Pérez-Montero (2014)

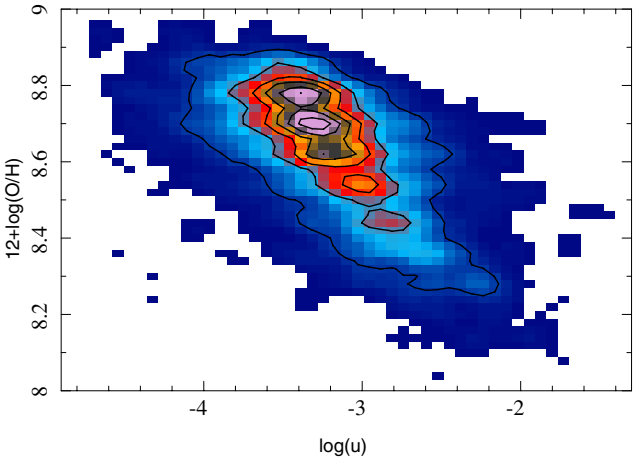

Fig. 3. Distribution of the oxygen abundance vs. ionization parameter for the ~5000 H II regions described in the text. The contours and color show the density distribution, with the outermost contour enclosing 95% of the regions, and each consecutive one enclosing 20% fewer regions.

clearly show that this relation is not induced by the strong-line calibrator used to derive the abundance.

As a sanity check, we repeated the figure using different abundance and ionization parameter estimators, and we found the same result for all of them. This trend cannot be explained purely by photoionization models, which assume that both parameters are totally independent.

We should note here that these representations of the data are dominated by the average properties, and they highlight the dominant trends. Secondary dependencies are mostly hidden or blurred when adopting this scheme and are appreciated only when the dominant trend is removed.

3.3. Distribution by galaxy morphology

In the previous sections, we have explored the distribution of the H II regions across the BPT diagram, comparing it with the predictions by photoionization models (Sect. 3.1) and the empirical estimation of a set of parameters that defines the ionization conditions (Sect. 3.2). Now we explore the dependence of the location of H II regions across the BPT diagram on the morphology of the host galaxy. The morphological classification was performed by eye, based on independent analysis by five members of the CALIFA collaboration, and it is described elsewhere in detail (Walcher et al. 2014). Different tests indicate that our morphological classification is fully compatible with pre-existing ones, and the results agree with the expectations based on other photometric or morphological parameters, such as the concentration index (Sánchez et al. 2013) or the Sersic index (Sersic 1968).

Figure 4 shows the distribution of H II regions across the BPT diagram separated by the morphology of their host galaxies. Each panel shows the H II regions corresponding to galaxies from earlier to later morphological types, divided into four groups with a similar number of galaxies in each one: (i) the top lefthand panel comprises those regions found in E/S0 and Sa galaxies (we found H II regions in only one galaxy classified as elliptical; however, 2/3 of the classifiers selected them as S0 in Walcher et al. 2014). (ii) The top righthand panel comprises those regions found in Sb galaxies. (iii) The bottom lefthand panel comprises those regions found in Sbc galaxies, and

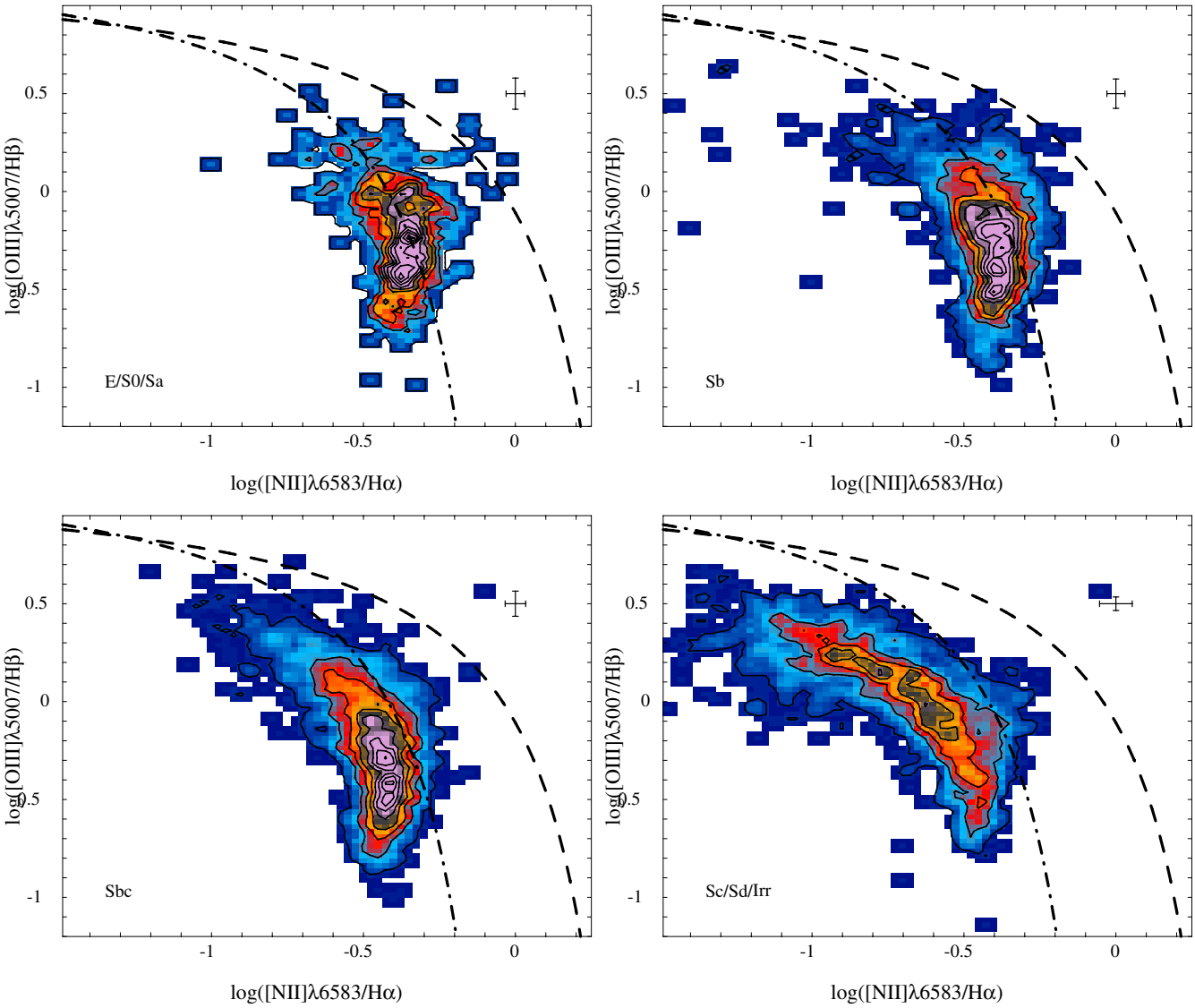

Fig. 4. [O III] λ5007/Hβ vs. [N II] λ6583/Hα diagnostic diagram for the ~5000 H II regions described in the text. The contours show the density distribution of these regions with the diagram plane, with the outermost contour enclosing 95% of the regions and each consecutive one enclosing 20% fewer regions. In each panel, H II regions corresponding to different galaxies with different morphological types are represented: (i) E/S0/Sa *top left*; (ii) Sb *top right*; (iii) Sbc *bottom left*; and (iv) Sc/Sd/Irr *bottom right panel*. In all panels, the dot-dashed and dashed lines represent the demarcation curves described in Fig. 1.

finally, (iv) the bottom righthand panel comprises those regions found in Sc/Sd and irregular galaxies.

There is a clear pattern in the distribution of H II regions across the BPT diagram depending on the morphology of the host galaxies. Early-type galaxies have H II regions located at the right end of the distribution. For those galaxies the number of regions within the intermediate area is much larger (~50% for E/S0 and Sa galaxies). Late-type galaxies have H II regions located along the classical sequence of these regions (e.g., Osterbrock 1989), with a clear trend toward more regions in the upper-left end of the distribution, the later the type of the galaxy.

A priori, we did not expect a connection between the location in the BPT diagram that is related to the ionization conditions of the nebulae and the morphological type of the host galaxies, since H II regions are short-lived phenomena. This result indicates that it is not possible to generate any kind of H II region in any morphological type. I.e., there is a connection between the feasible ionization conditions in a nebulae and the morphological type of the host galaxy.

3.4. Distribution by galactocentric distance

In the previous section we explored the distribution of the H II regions across the BPT diagram based on the morphological type of the host galaxies. In this section we explore the distribution of the H II regions based on their galactocentric distances.

To do so, we use the galactocentric distances normalized to the effective radius presented in Sánchez et al. (2013). Those distances have been derived from the catalog of H II regions provided by H IIEXPLORER (Sánchez et al. 2012b), corrected for the estimated inclination of the galaxy and normalized to the disk effective radius (see Appendix of Sánchez et al. 2013).

Figure 5 shows the distribution of H II regions across the BPT diagram distinguished by their galactocentric distances. Each panel shows the H II regions corresponding to galaxies from smaller to larger galactocentric distances, divided into four groups with a similar number of regions in each one: (i) the top lefthand panel shows the regions at $R/R_e < 0.5$; (ii) the top righthand panel those regions found between $0.5 < R/R_e < 1$;

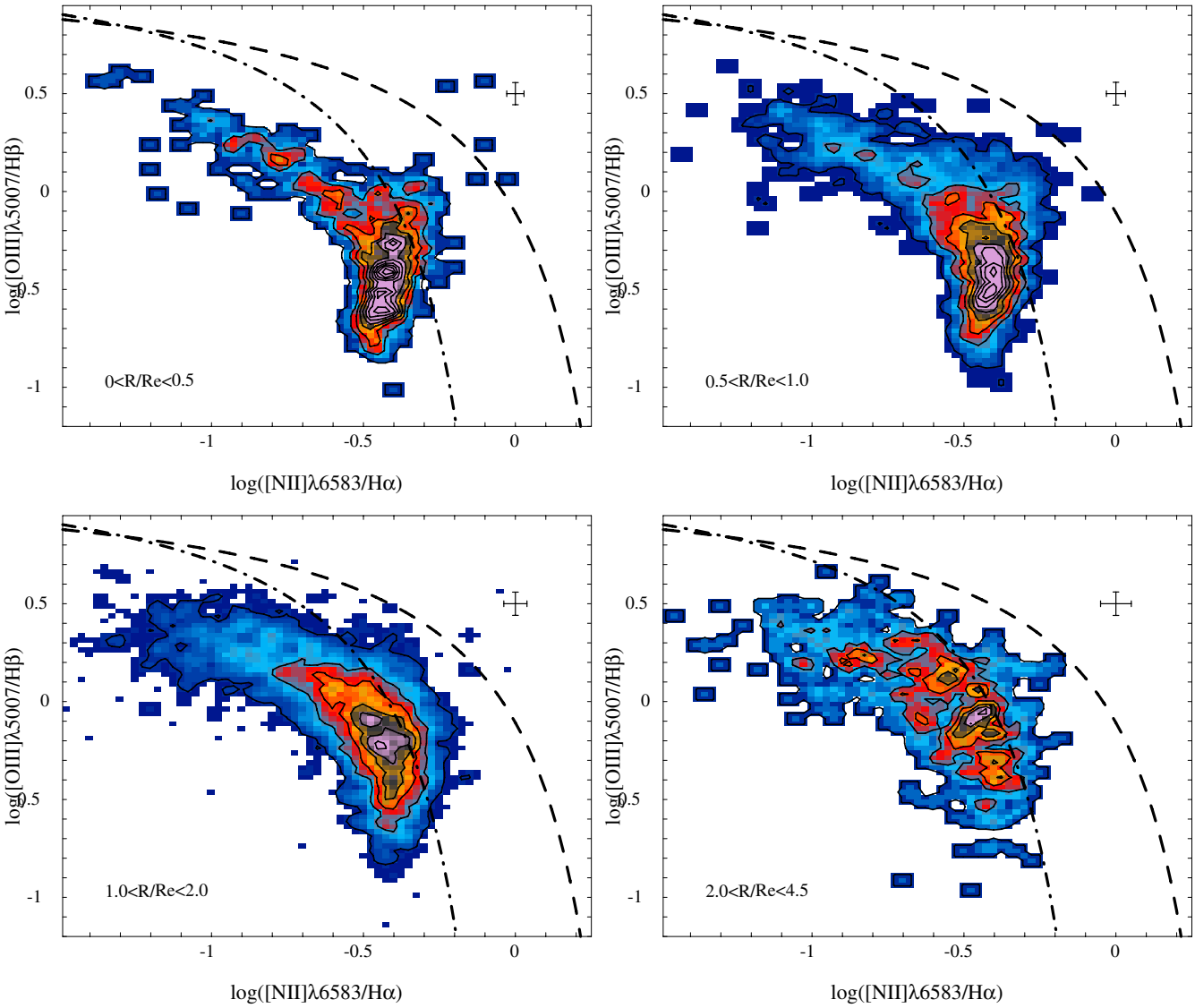

Fig. 5. [O III] λ5007/Hβ vs. [N II] λ6583/Hα diagnostic diagram for the ~5000 H II regions described in the text. The contours show the density distribution of these regions with the diagram plane, with the outermost contour enclosing 95% of the regions, and each consecutive one enclosing 20% fewer regions. Each panel shows the H II regions corresponding to different galactocentric distances, normalized to the effective radius: (i) $R/Re < 0.5$ *top left*; (ii) $0.5 < R/Re < 1.0$ *top right*; (iii) $1.0 < R/Re < 2.0$ *bottom left*; and (iv) $R/Re > 2.0$ *bottom right panel*. In all panels, the dot-dashed and dashed lines represent the demarcation curves described in Fig. 1.

(iii) the bottom lefthand panel those regions found between $1 < R/R_e < 2$; and finally, (iv) the bottom righthand panel those regions found at distances greater than $R/R_e > 2$.

There is a similar trend to the one described for the morphological type. The H II regions in the central areas of the galaxies are more frequently located at the right end of the distribution, with a larger number of them within the intermediate region. On the other hand, the H II regions in the outer regions follow a distribution that is more consistent with the classical trend (e.g., Osterbrock 1989). This is somewhat expected, since classical H II regions were observed in the disk of late-type spiral galaxies (e.g., Diaz 1989). However, as indicated before, Kennicutt et al. (1989) and Ho et al. (1997) recognized that H II regions in the center of galaxies distinguish themselves spectroscopically from those in the disk by their stronger low-ionization, forbidden emission lines. Initially it was thought that this may be due to contamination by an extra source of ionization, such as diffuse emission or the presence of an AGN. However, Sánchez et al. (2014) found that these regions are located across the entire optical extension of the galaxies, and most probably they are the consequence of a nitrogen enhancement due to a natural aging process of H II regions and the surrounding ISM.

3.5. Distribution by the properties of the underlying stellar population

In the two previous sections we explored the distribution of the H II regions across the BPT diagram based on the morphology of the host galaxy and the galactocentric distance of the considered region. We found that regions located in the central areas of galaxies, and in earlier type galaxies are located in the right and lower-right side of the distribution, while those regions located at larger galactocentric distances and in later-type galaxies are more frequently located toward the upper-left side of the distribution. Since the stellar population of the center of disk galaxies present similarities with that of early type galaxies (e.g., González Delgado et al. 2014b), these trends may indicate

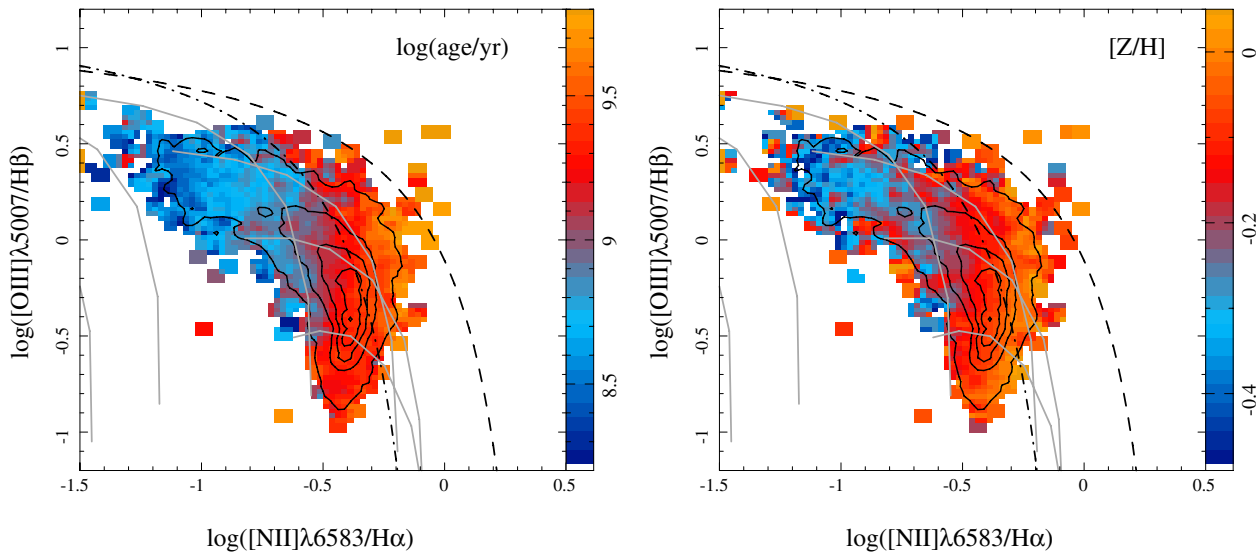

Fig. 6. [O III] λ5007/Hβ vs. [N II] λ6583/Hα diagnostic diagram for the ~5000 H II regions included in our sample. The contours show the density distribution of these regions within the diagram plane, with the outermost contour enclosing 95% of the regions, and each consecutive one enclosing 20% fewer regions. In each panel the color indicates the average value at the corresponding location in the diagram of the luminosity-weighted age (*left panel*) and metallicity (*right panel*) of the underlying stellar population, respectively. The gray solid lines represent the expected line ratios derived from the photoionization models shown in Fig. 1, where each line corresponds to a different stellar metallicity (orange-to-red solid lines in Fig. 1). In both panels, the dot-dashed and dashed lines represent the demarcation curves described in Fig. 1.

a connection between the location with the BPT diagram and the properties of the underlying stellar population.

We derive the luminosity-weighted ages and metallicities of the underlying stellar population for each H II region, adopting the results from the analysis described in Sánchez et al. (2013) and Sánchez et al. (2014), summarized before. The lefthand panel of Fig. 6 shows the distribution of H II regions across the BPT diagram with a color code representing the age of the underlying stellar population. Those regions with older underlying stellar population are located at the right/lower-right end of the distribution, while those with younger underlying stellar populations are located at the upper-left side. We should note here that we are not talking about the age of the ionizing population, the derivation of which would require a more detailed analysis (e.g., Miralles-Caballero et al. 2014), but the complete stellar population at the location of each H II region.

The righthand panel of Fig. 6 shows the distribution of H II regions across the BPT diagram with a color code representing the metallicity of the underlying stellar population, in units of [Z/H] (=log($Z/Z_\odot$), where $Z_\odot$ = 0.02). Those regions with metal-rich underlying stellar populations are located at the right/lower-right end of the distribution, while the metal poor ones are at the upper-left side. Despite the larger scatter this trend is very similar to the one presented in Fig. 2 for the oxygen abundance, indicating a correspondence between the oxygen abundance and the stellar metallicity of the underlying population. This correspondence has been recently described by González Delgado et al. (2014a) and Sanchez-Blazquez et al. (2014) in two independent analyses of the same data.

We should recall again that these representations of the data are dominated by the average properties, and they highlight the dominant trends. For example, the left-to-right gradient of the age seen in the lefthand panel of Fig. 6 should not be interpreted as a lack of dependence of [O III] on this parameter. The correct interpretation is that the dependence of [N II] with the age is much stronger, as we see in the next section.

3.6. Correlations with the properties of the underlying stellar population

The trends described in the previous section across the BPT diagram with the properties of the underlying stellar population point toward some kind of relationship between them and the line ratios shown in the diagram. We explored these relations in the current section. The lefthand panel of Fig. 7 shows the distribution of the [N II]/Hα line ratio along the luminosity-weighted age of the underlying stellar population for the H II regions shown in the previous figures, with the stellar metallicity represented by a color code. There is a clear correlation between both parameters with a correlation coefficient of r = 0.58. This correlation depends on the abundance, since it is stronger for the higher metallicities (r = 0.70 for the super-solar metallicities). In general, the older and more metal rich the underlying stellar population, the higher the value of the [N II]/Hα line ratio.

To illustrate the described correlation more clearly we split the data into bins of increasing metallicity with a width of 0.1 dex in [Z/H] for each one and derived the mean value of the line ratio for different ages, separated by 0.25 dex in the logarithm of the age. The result is shown in Fig. 7, where the distribution of the mean line ratios (colored circles) as a function of the ages for each stellar metallicity are presented. The described depedence of the line ratio on both parameters is clearly seen.

To first order the, [N II]/Hα line ratio could thus be described as a linear combination of both the luminosity-weighted ages and metallicities of the underlying stellar population, for which the best fitting linear regression is

$$\log\left(\frac{[\mathrm{N\,II}]}{\mathrm{H}\alpha}\right) = 0.24\,\log(\mathrm{age/yr}) + 0.34\,[Z/\mathrm{H}] - 2.67. \quad (3)$$

After correcting for this dependency, the standard deviation of the line ratio is reduced by ~70%. Indeed, the dispersion around the best fitted surface of ~0.14 dex is similar to the mean error of the considered line ratio ~0.13 dex, compared with the initial dispersion (~0.20 dex). This indicates that the underlying stellar

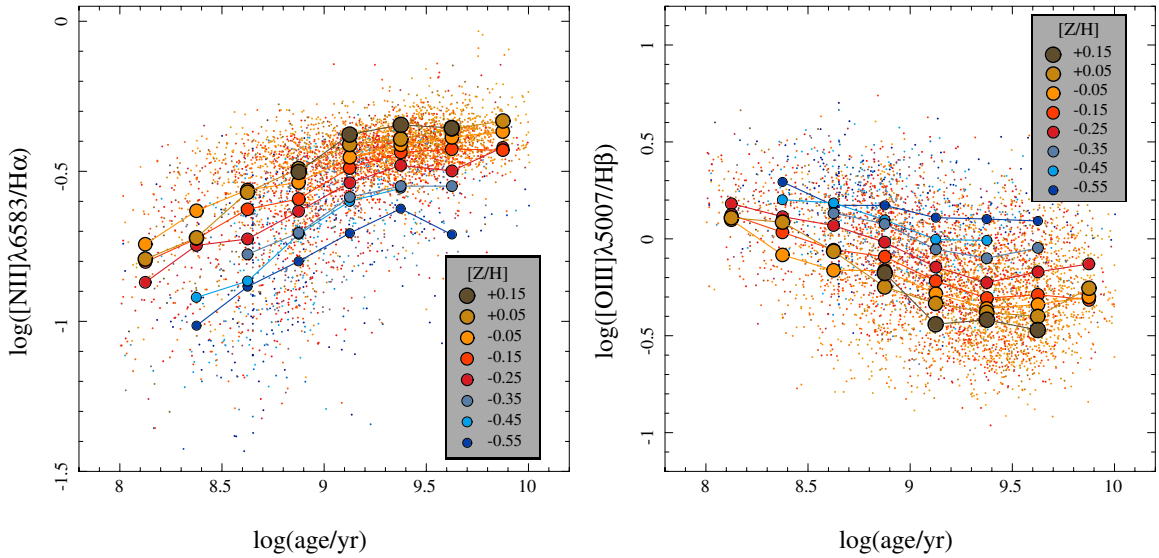

Fig. 7. *Left panel*: distribution of the [N II] λ6583/Hα line ratio along the luminosity-weighted ages of the underlying stellar population for the ~5000 H II regions included in our sample (individual dots), with a color code representing the luminosity weighted metallicity of the underlying stellar population. The solid circles and individual lines illustrate how the considered ratio change along the stellar population age for a certain metallicity range. Each circle represents the average line ratio within a bin of 0.25 dex in log(age/yr) for a fixed range of metallicities (within a range of 0.1 dex). Consecutive circles for a particular metallicity are linked with a solid line, and both of them are represented by a fixed color, different for each metallicity. The actual value of the metallicity corresponding to each color is indicated in the enhanced box. *Right panel*: similar distribution for the [O III] λ5007/Hβ line. Symbols, solid lines, and color codes are the same as presented in the previous panel.

population dominates the definition of the [N II]/Hα line ratio, and any other physical conditions of the nebulae seem to have little effect on it.

The righthand panel of Fig. 7 shows the distribution of the [O III]/Hβ line ratio along the luminosity-weighted age of the underlying stellar population in our H II region sample with the stellar metallicity represented with a color code. The correlation between both parameters is weaker than the one found for [N II]/Hα with a correlation coefficient of $r = 0.42$. As in the previous case, there is a dependency of this correlation on the abundance, because it is stronger for the higher metallicities ($r = 0.60$ for the super-solar metallicities). The double dependence is more evident when it is applied using the binning procedure for metallicity ranges and ages described before for [N II]/Hα.

In general, the younger and more metal poor the underlying stellar population, the higher the value of the [O III]/Hβ line ratio (unlike the expected for the ionizing stellar population). The best fitting linear regression between this line ratio and the properties of the underlying stellar population is described by the formula

$$\log\left(\frac{[\mathrm{O\,III}]}{\mathrm{H}\beta}\right) = -0.25\ \log(\mathrm{age/yr}) - 0.41\ [\mathrm{Z/H}] + 2.11. \quad (4)$$

After being corrected for this dependency, the standard deviation of the distribution of [O III]/Hβ decreases only by ~55%. For this line ratio the dispersion around the best fitted surface (~0.25 dex) is considerably larger than the mean error of the considered line ratio (~0.13 dex). In contrast to [N II]/Hα, it seems that the value of [O III]/Hβ not only depends on the underlying stellar population, but also seems to be sensitive to additional physical conditions in the nebulae, such as the age of the ionizing population, the electron density, the mass of the ionizing cluster, and the geometry of the ionized gas (e.g., Garcia-Vargas et al. 1995a).

We repeated all the analysis using the luminosity-weighted ages and metallicities derived using STARLIGHT, as described in González Delgado et al. (2014b) for the galaxies in common (~60% of the sample). These values are derived from a more detailed analysis of the underlying stellar population, using a larger and more suitable SSP library. We derived very similar results. The trend with the age of the underlying stellar population is exactly the same, while the trend with metallicity seems to be slighly weaker. However, this later result seems to be the effect of the smaller statiscal number of points rather than a real difference.

4. Discussion

So far we have explored the distribution of H II regions across the BPT diagram based on (i) the expected distributions derived from photoionization models; (ii) an estimated set of parameters defining the ionization conditions; (iii) the morphology of the host galaxies; (iv) the galactocentric distances of the H II regions; and (v) the main properties of the underlying stellar population. We found that the location of an H II region is not uniquely defined by a single set of parameters for any set of photoionization models; that is to say, their location in the BPT diagram could be reproduced by the models using different ionization conditions with a clear degenerancy between the ionization parameter, log(u) and the oxygen abundance. On the other hand, not all the possible locations predicted by photoionization models are covered by the observed H II regions (i.e., there are plausible combinations of physical parameters in H II regions which can be empirically excluded on the basis of the derived BPT diagrams). In summary, from all the feasible hyperspace of line ratios predicted by photoionization models, real H II regions cover a reduced region in this space, which is not predicted by the models.

Indeed, this result is not new. Other authors have previously noticed that from all the line ratios predicted by photoionization models, observed H II regions cover only a particular set of them (e.g., Dopita et al. 2000; Kewley et al. 2001). However, our larger statistical sample ensures that we can cover a much

wider range of ionization conditions, and the results still hold. Thus, there are ionization conditions described by photoionization models that are not found in real H II regions. This basically means that the observed H II regions are restricted to a particular set of parameters among those explored by photoionization models.

Furthermore, H II regions cover not only a particular region in the hyperspace of possible ionization conditions. We found that there are clear trends across the BPT diagram depending on the parameters defining the ionization. H II regions in the upper-left side of the diagram are more metal poor, with higher ionization strengths, and less dust attenuation than those regions in the right and lower-right end of the diagram. Again, we are not the first to notice this effect. Classical studies have already found similar trends for more reduced number of regions and/or fewer galaxies (Evans & Dopita 1985; Dopita & Evans 1986). More recently Bresolin et al. (2012) described the same trend of the ionization parameter across the BPT diagram for their sample of H II regions. Indeed, these trends are behind some of the well-known empirical calibrators between the oxygen abundance and the strong-line ratios, such as O3N2 (Alloin et al. 1979; Pettini & Pagel 2004; Stasińska et al. 2006; Marino et al. 2013) or N2 (Pettini & Pagel 2004; Marino et al. 2013). Dopita & Evans (1986) have already found that all the abundance calibrators based on strong line indicators break the degenerancy between the ionization parameter and the abundance existing in photoionization models based on the existence of an empirical correlation between both parameters. Indeed, Pérez-Montero (2014) have recently demonstrated that in the absence of this relation, it is not possible to derive a sensitive abundance based on any combination of strong emission line ratios, even for the largest dataset of H II regions with direct abundance estimations. The correlation described by Pérez-Montero (2014) is very similar to the one presented in Fig. 3.

Several explanations have been proposed for the relation between the oxygen abundance and the ionization parameter: (i) a correlation between the IMF and the metallicity and/or the ionization parameter (Dopita et al. 2006b). (ii) The correlation is the result of the dust absorption, and (iii) there are environmental effects that change the geometry of the H II regions at higher metallicities. The first possibility was discussed by Evans & Dopita (1985), without finding a conclusive result. The last two were discussed by Dopita & Evans (1986), who considered that the dust extinction required to produce the observed correlation should be greater than the observed one. Finally, they considered that the third may be possible if the correlation is related to a radial gradient in the density of the H II regions, with inner regions being more dense. However, as we have shown in Figs. 2 and 5, the electron density does not seem to present an obvious radial distribution and it does not present a clear correlation with the other two parameters.

A possible alternative explanation of this relation could be that for any given age, the ionizing stellar population becomes redder for higher metallicities. First, as the metallicity of the stars increases, so does the envelope opacity, causing a drop in their effective temperatures and a shift of flux toward redder wavelengths (e.g., Pagel & Edmunds 1981). Second, the ultraviolet emission is strongly influenced by metal line blanketing in the stellar atmospheres (e.g., Lanz & Hubeny 2003). Its effect is not as straight forward as the one of the opacity. Mokiem et al. (2004) found that the total number of Lyman continuum photons emitted is almost independent of line blanketing effects and metallicity for a given effective temperature. This is because the flux that is blocked by the forest of metal lines at wavelengths shorter than 600 Å is redistributed mainly within the Lyman continuum. However, they also find that blanketing produces a significant decrease in the effective temperature, as previously reported by Martins et al. (2002). Thus the net effect is a decrease in the Lyman photons with the metallicity (e.g., Lanz & Hubeny 2003).

Indeed, evolutionary models for giant H II regions describe a decrease in the ionization parameter with the metallicity for any given age and mass of the ionizing cluster qualitatively similar to the one described here (Garcia-Vargas et al. 1995a,b). The detailed dependency between both parameters is different for each age and mass of the ionizing cluster, as can be derived from the trends between emission lines shown in Martín-Manjón et al. (2010), and therefore a considerable scatter is expected in the described relation (as observed in Fig. 3).

Finally, the correlation may be induced by a totally different mechanism. Dopita et al. (2006a) propose a scenario in which the expansion and internal pressure of the ionized cloud is driven by the net input of mechanical energy from the central cluster (owing to winds of supernove events). Those models explain the anticorrelation of ionization parameter with the oxygen abundance naturally: (i) The stellar wind has a higher opacity for more metal-rich clouds and therefore absorbs a greater fraction of the ionizing photons, reducing $\log(u)$ in the surrounding H II region. (ii) The atmosphere scatters the photons emitted from the photosphere more efficiently when the atmospheric abundances are higher, leading to a greater conversion efficiency from luminous energy flux to mechanical energy flux in the stellar wind base region. This also leads to decreasing $\log(u)$ in the surrounding H II region.

The distribution shown in Fig. 4 is connected to the one shown in the upper lefthand panel of Fig. 2, via the $\mathcal{M}$-Z relation (Tremonti et al. 2004; Sánchez et al. 2013). Early-type galaxies are, in general, more massive and therefore more metal rich than late-type ones, therefore their H II regions are located toward the right/lower-right end of the distribution. On the other hand, the H II regions of latter-type galaxies, more metal poor, are located toward the left/upper-left side. The distribution shown in Fig. 5 can be explained based on the well known inverse galactocentric abundance gradient, which seems to be present in all galaxy types (e.g., Sánchez et al. 2012b, 2014, and references therein). Indeed, both distributions can also be explained based on Σ-Z relation (Rosales-Ortega et al. 2012; Sánchez et al. 2013), since the central regions of galaxies present higher stellar mass densities, hence larger oxygen abundances. Thus, the location of H II regions within the BPT diagram changes with the morphology and the galactocentric distance owing to the described trend between this location and the oxygen abundance.

The trend found for the dust attenuation was not a consequence of the dependence of the line ratios on dust attenuation, and it was not predicted by the adopted photoionization models. By construction the location within the BPT diagram should be indepedent of this parameter (Fig. 2, bottom right-hand panel). Based on the previous results, this trend indicates that there should be an inverse gradient of the dust attenuation with the galactocentric distance and a relation with the stellar mass density, similar to the ones described for the oxygen abundance. To our knowledge these trends have not been reported. In Sánchez et al. (2012b) we found only a very weak inverse galactocentric gradient of the dust attenuation for a reduced sample of face-on spiral galaxies. However, that sample was dominated by Sc/Sd galaxies, which may have affected the results. Similar results for individual objects were presented by López-Sánchez et al. (2004, 2006) and Monreal-Ibero et al. (2010).

A possible explanation for this trend could arise from the known relation between the stellar dust attenuation and the H I gas surface density (Bohlin et al. 1978). Since gas and stellar attenuations present a tight relation (e.g., Calzetti et al. 1994; Calzetti 2001), there should a correlation between the dust attenuation in the gas and the gas mass density, as recently highlighted by Brinchmann et al. (2013). Since the gas surface density increases toward the center of spiral galaxies (e.g., Young & Scoville 1991), it is expected that there will be a corresponding increase in A_V, gas in the inner regions. On the other hand, this trend could be a consequence of the relation between metals and the dust grains, and therefore, between metals and dust attenuation. Thanks to this relation the dust-to-gas ratio increases with metallicity, as nicely summarized by Brinchmann et al. (2013). Indeed, for the Milky Way it is about three times greater than for the Large Magellanic Cloud and ~1.5 times greater than for the Small Magellanic Cloud, as a direct consequence of the differences in metallicity between these three galaxies (e.g., Bohlin et al. 1978; Fitzpatrick 1986; Rodrigues et al. 1997). In this case the galactocentric decrease of the abundance may induce a similar gradient for the dust attenuation.

Finally, the trend described for the electron density seems to be explained naturally by photoionization models (Fig. 2, bottom lefthand panel). Indeed, Kewley et al. (2013) have nicely illustrated this effect recently (e.g., their Fig. 2). Electron density is a proxy of the ionized gas density, which is susceptible to modifications owing to different dynamical mechanisms that modified the pressure. In an isobaric density distribution, the density is defined in terms of the ratio of the mean ISM pressure, P, and the mean electron temperature, T_e, through $n_e = P/T_e k$. For the typical electron temperature of ionized gas, the density is simply determined by the ISM pressure (Kewley et al. 2013). Some authors have described a radial trend in the electron density in spiral galaxies (e.g., Gutiérrez & Beckman 2010; Beckman et al. 2013), although it has not been tested in a statistically significant large sample of galaxies. It is also expected that the electron density increases in the wave front of spiral arms (e.g., Gutiérrez & Beckman 2010), and due to external effects, like galaxy interaction (e.g., Krabbe et al. 2014).

Highly active star-forming galaxies, like ULIRGs, and high redshift ones, both with dense ionized gas, are known to be located at the upper end of the classical location for H II regions (e.g., Brinchmann et al. 2008; Lehnert et al. 2009; Yuan et al. 2010; Dopita et al. 2014), in agreement with our result. Finally, the electron density could evolve with the age of the ionizing cluster if we assume that H II region is evolving as a mass-loss bubble pressurized by the combined ram pressure of the stellar wind and supernova explosions (Dopita et al. 2014), as decribed before. In this scenario the density and the radius of the H II regions are closely coupled, and both of them depend on the age of the ionizing cluster. Under this assumptions, we expect a variation in the electron density across the optical extension of the galaxies.

All these results indicate that the location within the BPT diagram is tightly related to properties of the underlying stellar population. Indeed, Fig. 7 shows that both line ratios involved in the BPT diagram present clear correlations with the age and metallicity of the stellar populations. In particular, the [N II] λ6583/Hα value is totally defined by both parameters within the errors. This is somewhat expected since this line ratio is a proxy of the oxygen abundance (e.g., Marino et al. 2013). Since the gas is polluted by the last population of stars, and assuming that the radial mixing is not too strong – which can be assumed based on the results by Sánchez et al. (2014) and Sanchez-Blazquez et al. (2014) – the oxygen abundance has to be correlated with the metallicity of the younger population of stars. Indeed, the gas abundance should be the envelope of the distribution of metallicities within the underlying stellar population (as recently found by González-Delgado et al. 2014b). Therefore, a correlation between the abundance and the metallicity is expected for two reasons: both the ionizing stars, the youngest ones, should be more metal-rich, and the ionized gas should be polluted by the last generation of metal-rich stars.

The correlation with the age is a consequence of the chemical enrichment in galaxies. We know that disk-dominated galaxies grow inside out, with the older and more metal-rich stellar populations living in the central regions, where the stellar mass density is higher (e.g., Pérez et al. 2013; González Delgado et al. 2014b; Sanchez-Blazquez et al. 2014). Therefore, a correlation between the oxygen abundance of the H II regions and the age of the underlying stellar population is expected, therefore between this parameter and [N II] λ6583/Hα.

Finally, for [O III] λ5007/Hβ, it is also expected that the correlation is weaker. This line ratio is less sensitive to the metallicity. The excitation of O^{++} requires a much higher energy than for of N^{+}, and therefore it is more sensitive to variations in the geometry of the nebulae, the gas density, and the properties of the ionizing population. Although this also has the imprint of the local chemical evolution of the galaxy, owing to its metal content, its evolution affects this line ratio more than the former one. The location within the BPT diagram is largely explained, therefore, by the chemical enrichment and star-formation history, but not totally.

Throughout this article we have explored the dependence of the location of H II regions within the BPT diagram with the properties of the underlying stellar population. We selected the BPT diagram as the archetype of the diagnostics diagrams, on one hand, and because the line ratios involved are less sensitive to dust attenuation. However, the main results described in this article would be similar if other diagnostic diagrams were used. In Appendix A, we illustrate how the distribution of H II regions across other broadly used diagnostic diagrams depends on the properties of the underlying stellar population. For clarity we prefer not to present them in the main text.

5. Summary and conclusions

In this study we have presented the distribution across the BPT diagram for the largest catalog of H II regions with the spectroscopic information currently available (Sánchez et al. 2013, 2014). We compared their location in this diagram to what is predicted by photoionization models, finding that (i) H II regions do not cover the entire range of parameters predicted by these models; and (ii) the same location within the diagram can be reproduced by several combinations of ionization parameters and photoionization models, in many cases.

We showed that these parameters (ionization parameter, oxygen abundance, electron density, and dust attenuation) follow well-defined trends across the BPT diagram. Only the trend described for the electron density can be explained directly by photoionization models. The remaining trends must have a different origin. Indeed, there is clear correlation between the ionization parameter and the oxygen abundance that cannot be explained based on photoinization models. Different explanations for this correlation, extracted from the literature, have been discussed. We proposed an alternative one, in which the relation is a consequence of the increase in the metal line blanketing and the envelope opacity of the ionizing stars with the metallicity.

We found that the location of H II regions within the BPT diagram depends to first order on the morphology of the host galaxy, the galactocentric distance, and ultimately, the properties of the underlying stellar population (age and metallicity). The reason for these empirical trends are related to the chemical evolution in galaxies. Oxygen abundance is a tracer of stellar metallicity, hence a byproduct of the star-formation history and metal enrichment. For this reason, the metal-sensitive line ratios are tighly correlated with the properties of the underlying stellar population (i.e., the products of the SFH). Finally, owing to the correlation between the oxygen abundance and the ionizing parameter, those line ratios more sensitive to this latter physical quantity depend on the properties of the underlying stellar population, too.

Even though H II regions are short-lived phenomena, their ionization conditions seem to be tightly related to the properties of the underlying stellar population; i.e., they keep a memory of the local star-formation history and metal enrichment at the location where they are formed.

Acknowledgements. We thank Prf. Dr. M. Dopita for his comments and suggestions during the reviewing process. He helped to improve significantly the interpretation of our results and the overall manuscript. S.F.S. thanks the director of CEFCA, M. Moles, for his sincere support to this project. This study makes uses of the data provided by the Calar Alto Legacy Integral Field Area (CALIFA) survey (http://califa.caha.es/). CALIFA is the first legacy survey being performed at Calar Alto. The CALIFA collaboration would like to thank the IAA-CSIC and MPIA-MPG as major partners of the observatory and CAHA itself, for the unique access to telescope time and support in manpower and infrastructures. The CALIFA collaboration also thanks the CAHA staff for the dedication to this project. This work was based on observations collected at the Centro Astronómico Hispano Alemán (CAHA) at Calar Alto, operated jointly by the Max-Planck-Institut für Astronomie and the Instituto de Astrofísica de Andalucia (CSIC). We thank the Viabilidad, Diseño, Acceso y Mejora funding program, ICTS-2009-10, for supporting the initial developement of this project. S.F.S. thanks the ConaCyt funding program 180125, for the support given to this project. S.F.S., M.A.M. and L.S.M. thank the Plan Nacional de Investigación y Desarrollo funding programs, AYA2012-31935, of the Spanish Ministerio de Economía y Competitividad, for the support given to this project. S.F.S. thanks the Ramón y Cajal project RyC-2011-07590 of the Spanish Ministerio de Economía y Competitividad, for its support of this project. P.P. is supported by a FCT Investigator 2013 consolidation grant. He acknowledges support by the Fundação para a Ciência e a Tecnologia (FCT) under project FCOMP-01-0124-FEDER-029170 (Reference FCT PTDC/FIS-AST/3214/2012), funded by FCT-MEC (PIDDAC) and FEDER (COMPETE). R.G.D., E.P., and R.G.B. thank the Plan Nacional de Investigación y Desarrollo funding program AYA2010-15081. Support for LG is provided by the Ministry of Economy, Development, and Tourism's Millennium Science Initiative through grant IC12009, awarded to The Millennium Institute of Astrophysics, MAS. L.G. acknowledges support by CONICYT through FONDECYT grant 3140566. R.A. Marino was also funded by the Spanish program of International Campus of Excellence Moncloa (CEI). A. M.-I. acknowledges support from Agence Nationale de la Recherche through the STILISM project (ANR-12-BS05-0016-02).

References

Allen, M. G., Groves, B. A., Dopita, M. A., Sutherland, R. S., & Kewley, L. J. 2008, ApJS, 178, 20
Alloin, D., Collin-Souffrin, S., Joly, M., & Vigroux, L. 1979, A&A, 78, 200
Anderson, L. D. 2014, American Astronomical Society Meeting Abstracts, 223, 31201
Baldwin, J. A., Phillips, M. M., & Terlevich, R. 1981, PASP, 93, 5
Beckman, J. E., Cedrés, B., Giammanco, C., Bongiovanni, A., & Cepa, J. 2013, Rev. Mex. Astron. Astrofis. Conf. Ser., 42, 14
Binette, L., Magris, C. G., Stasińska, G., & Bruzual, A. G. 1994, A&A, 292, 13
Binette, L., Flores-Fajardo, N., Raga, A. C., Drissen, L., & Morisset, C. 2009, ApJ, 695, 552
Bohlin, R. C., Savage, B. D., & Drake, J. F. 1978, ApJ, 224, 132
Bresolin, F., Ryan-Weber, E., Kennicutt, R. C., & Goddard, Q. 2009, ApJ, 695, 580
Bresolin, F., Kennicutt, R. C., & Ryan-Weber, E. 2012, ApJ, 750, 122
Brinchmann, J., Pettini, M., & Charlot, S. 2008, MNRAS, 385, 769
Brinchmann, J., Charlot, S., Kauffmann, G., et al. 2013, MNRAS, 432, 2112
Cairós, L. M., Caon, N., García Lorenzo, B., et al. 2012, A&A, 547, A24
Calzetti, D. 2001, PASP, 113, 1449
Calzetti, D., Kinney, A. L., & Storchi-Bergmann, T. 1994, ApJ, 429, 582
Cardelli, J. A., Clayton, G. C., & Mathis, J. S. 1989, ApJ, 345, 245
Cid Fernandes, R., Stasińska, G., Schlickmann, M. S., et al. 2010, MNRAS, 403, 1036
Cid Fernandes, R., Perez, E., Garcia Benito, R., et al. 2013, A&A, 557, A86
Cid Fernandes, R., González Delgado, R. M., García Benito, R., et al. 2014, A&A, 561, A130
Diaz, A. I. 1989, in Evolutionary Phenomena in Galaxies, eds. J. E. Beckman, & B. E. J. Pagel (Cambridge, New York: Cambridge University Press), 377
Díaz, A. I., Castellanos, M., Terlevich, E., & Luisa García-Vargas, M. 2000, MNRAS, 318, 462
Dopita, M. A., & Evans, I. N. 1986, ApJ, 307, 431
Dopita, M. A., & Sutherland, R. S. 1995, ApJ, 455, 468
Dopita, M. A., Kewley, L. J., Heisler, C. A., & Sutherland, R. S. 2000, ApJ, 542, 224
Dopita, M. A., Fischera, J., Sutherland, R. S., et al. 2006a, ApJS, 167, 177
Dopita, M. A., Fischera, J., Sutherland, R. S., et al. 2006b, ApJ, 647, 244
Dopita, M. A., Sutherland, R. S., Nicholls, D. C., Kewley, L. J., & Vogt, F. P. A. 2013, ApJS, 208, 10
Dopita, M. A., Rich, J., Vogt, F. P. A., et al. 2014, Ap&SS, 350, 741
Dors, Jr., O. L., Krabbe, A., Hägele, G. F., & Pérez-Montero, E. 2011, MNRAS, 415, 3616
Dottori, H. A. 1987, Rev. Mex. Astron. Astrofis., 14, 463
Dottori, H. A., & Copetti, M. V. F. 1989, Rev. Mex. Astron. Astrofis., 18, 115
Evans, I. N., & Dopita, M. A. 1985, ApJS, 58, 125
Falcón-Barroso, J., Sánchez-Blázquez, P., Vazdekis, A., et al. 2011, A&A, 532, A95
Fitzpatrick, E. L. 1986, AJ, 92, 1068
Flores-Fajardo, N., Morisset, C., Stasińska, G., & Binette, L. 2011, MNRAS, 415, 2182
García-Benito, R., Pérez, E., Díaz, Á. I., Maíz Apellániz, J., & Cerviño, M. 2011, AJ, 141, 126
Garcia-Vargas, M. L., Bressan, A., & Diaz, A. I. 1995a, A&AS, 112, 13
Garcia-Vargas, M. L., Bressan, A., & Diaz, A. I. 1995b, A&AS, 112, 35
Garnett, D. R. 2002, ApJ, 581, 1019
González Delgado, R. M., & Perez, E. 1997, ApJS, 108, 199
González Delgado, R. M., Cid Fernandes, R., García-Benito, R., et al. 2014a, ApJ, 791, L16
González Delgado, R. M., Pérez, E., Cid Fernandes, R., et al. 2014b, A&A, 562, A47
Gutiérrez, L., & Beckman, J. E. 2010, ApJ, 710, L44
Ho, L. C., Filippenko, A. V., & Sargent, W. L. W. 1997, ApJ, 487, 579
Hodge, P. W., & Kennicutt, Jr., R. C. 1983, ApJ, 267, 563
Husemann, B., Jahnke, K., Sánchez, S. F., et al. 2013, A&A, 549, A87
Kauffmann, G., Heckman, T. M., Tremonti, C., et al. 2003, MNRAS, 346, 1055
Kehrig, C., Vílchez, J. M., Sánchez, S. F., et al. 2008, A&A, 477, 813
Kehrig, C., Monreal-Ibero, A., Papaderos, P., et al. 2012, A&A, 540, A11
Kelz, A., Verheijen, M. A. W., Roth, M. M., et al. 2006, PASP, 118, 129
Kennicutt, Jr., R. C., Keel, W. C., & Blaha, C. A. 1989, AJ, 97, 1022
Kewley, L. J., Dopita, M. A., Leitherer, C., et al. 2013, ApJ, 774, 100
Kewley, L. J., Dopita, M. A., Sutherland, R. S., Heisler, C. A., & Trevena, J. 2001, ApJ, 556, 121
Kewley, L. J., Groves, B., Kauffmann, G., & Heckman, T. 2006, MNRAS, 372, 961
Knapen, J. H. 1998, MNRAS, 297, 255
Krabbe, A. C., Rosa, D. A., Dors, O. L., et al. 2014, MNRAS, 437, 1155
Lanz, T., & Hubeny, I. 2003, ApJS, 146, 417
Lehnert, M. D., Nesvadba, N. P. H., Le Tiran, L., et al. 2009, ApJ, 699, 1660
Lequeux, J., Peimbert, M., Rayo, J. F., Serrano, A., & Torres-Peimbert, S. 1979, A&A, 80, 155
Lopez, L. A., Krumholz, M. R., Bolatto, A. D., Prochaska, J. X., & Ramirez-Ruiz, E. 2011, ApJ, 731, 91
López-Sánchez, A. R., & Esteban, C. 2009, A&A, 508, 615
López-Sánchez, Á. R., Esteban, C., & Rodríguez, M. 2004, A&A, 428, 425
López-Sánchez, Á. R., Esteban, C., & García-Rojas, J. 2006, A&A, 449, 997
Marino, R. A., Gil de Paz, A., Castillo-Morales, A., et al. 2012, ApJ, 754, 61
Marino, R. A., Rosales-Ortega, F. F., Sánchez, S. F., et al. 2013, A&A, 559, A114
Martin, P., & Roy, J.-R. 1994, ApJ, 424, 599
Martín-Manjón, M. L., García-Vargas, M. L., Mollá, M., & Díaz, A. I. 2010, MNRAS, 403, 2012
Martins, F., Schaerer, D., & Hillier, D. J. 2002, A&A, 382, 999
Mast, D., Rosales-Ortega, F. F., Sánchez, S. F., et al. 2014, A&A, 561, A129
McCall, M. L., Rybski, P. M., & Shields, G. A. 1985, ApJS, 57, 1
Miralles-Caballero, D., Díaz, A. I., Rosales-Ortega, F. F., Pérez-Montero, E., & Sánchez, S. F. 2014, MNRAS, 440, 2265

Mokiem, M. R., Martín-Hernández, N. L., Lenorzer, A., de Koter, A., & Tielens, A. G. G. M. 2004, A&A, 419, 319
Monreal-Ibero, A., Vílchez, J. M., Walsh, J. R., & Muñoz-Tuñón, C. 2010, A&A, 517, A27
Monreal-Ibero, A., Relaño, M., Kehrig, C., et al. 2011, MNRAS, 413, 2242
Morisset, C., & Georgiev, L. 2009, A&A, 507, 1517
Moustakas, J., & Kennicutt, Jr., R. C. 2006, ApJS, 164, 81
Oey, M. S., Parker, J. S., Mikles, V. J., & Zhang, X. 2003, AJ, 126, 2317
Osterbrock, D. E. 1989, Astrophysics of gaseous nebulae and active galactic nuclei (University Science Books)
Pagel, B. E. J., & Edmunds, M. G. 1981, ARA&A, 19, 77
Papaderos, P., Gomes, J. M., Vilchez, J. M., et al. 2013, A&A, 555, L1
Pérez, E., Cid Fernandes, R., González Delgado, R. M., et al. 2013, ApJ, 764, L1
Pérez-Montero, E. 2014, MNRAS, 441, 2663
Pettini, M., & Pagel, B. E. J. 2004, MNRAS, 348, L59
Pilyugin, L. S., Vílchez, J. M., & Thuan, T. X. 2010, ApJ, 720, 1738
Pilyugin, L. S., Grebel, E. K., & Mattsson, L. 2012, MNRAS, 424, 2316
Relaño, M., Monreal-Ibero, A., Vílchez, J. M., & Kennicutt, R. C. 2010, MNRAS, 402, 1635
Rodrigues, C. V., Magalhães, A. M., Coyne, G. V., & Piirola, S. J. V. 1997, ApJ, 485, 618
Rosales-Ortega, F. F., Kennicutt, R. C., Sánchez, S. F., et al. 2010, MNRAS, 405, 735
Rosales-Ortega, F. F., Díaz, A. I., Kennicutt, R. C., & Sánchez, S. F. 2011, MNRAS, 415, 2439
Rosales-Ortega, F. F., Sánchez, S. F., Iglesias-Páramo, J., et al. 2012, ApJ, 756, L31
Roth, M. M., Kelz, A., Fechner, T., et al. 2005, PASP, 117, 620
Sánchez, S. F., Becker, T., Garcia-Lorenzo, B., et al. 2005, A&A, 429, L21
Sánchez, S. F., García-Lorenzo, B., Jahnke, K., et al. 2006, New Astron. Rev., 49, 501
Sánchez, S. F., Cardiel, N., Verheijen, M. A. W., et al. 2007, A&A, 465, 207
Sánchez, S. F., Rosales-Ortega, F. F., Kennicutt, R. C., et al. 2011, MNRAS, 410, 313
Sánchez, S. F., Kennicutt, R. C., Gil de Paz, A., et al. 2012a, A&A, 538, A8
Sánchez, S. F., Rosales-Ortega, F. F., Marino, R. A., et al. 2012b, A&A, 546, A2
Sánchez, S. F., Rosales-Ortega, F. F., Jungwiert, B., et al. 2013, A&A, 554, A58
Sánchez, S. F., Rosales-Ortega, F. F., Iglesias-Páramo, J., et al. 2014, A&A, 563, A49
Sanchez-Blazquez, P., Rosales-Ortega, F., Mendez-Abreu, J., et al. 2014, A&A, 570, A6
Sanduleak, N. 1969, AJ, 74, 47
Searle, L. 1971, ApJ, 168, 327
Sersic, J. L. 1968, Atlas de galaxias australes (Cordoba: Observatorio Astronomica)
Singh, R., van de Ven, G., Jahnke, K., et al. 2013, A&A, 558, A43
Skillman, E. D. 1989, ApJ, 347, 883
Stasińska, G., Cid Fernandes, R., Mateus, A., Sodré, L., & Asari, N. V. 2006, MNRAS, 371, 972
Tremonti, C. A., Heckman, T. M., Kauffmann, G., et al. 2004, ApJ, 613, 898
Vazdekis, A., Sánchez-Blázquez, P., Falcón-Barroso, J., et al. 2010, MNRAS, 404, 1639
Veilleux, S., & Osterbrock, D. E. 1987, ApJS, 63, 295
Veilleux, S., Kim, D.-C., Sanders, D. B., Mazzarella, J. M., & Soifer, B. T. 1995, ApJS, 98, 171
Vila-Costas, M. B., & Edmunds, M. G. 1992, MNRAS, 259, 121
Vogt, F. P. A., Dopita, M. A., Kewley, L. J., et al. 2014, ApJ, 793, 127
Walcher, C. J., Wisotzki, L., Bekeraité, S., et al. 2014, A&A, 569, A1
Yoachim, P., Roškar, R., & Debattista, V. P. 2010, ApJ, 716, L4
Young, J. S., & Scoville, N. Z. 1991, ARA&A, 29, 581
Yuan, T.-T., Kewley, L. J., & Sanders, D. B. 2010, ApJ, 709, 884
Zaritsky, D., Kennicutt, Jr., R. C., & Huchra, J. P. 1994, ApJ, 420, 87

Page 17 is available in the electronic edition of the journal at http://www.aanda.org

Appendix A: Distribution of H II regions across other diagnostic diagrams

This study has been focused on study how the imprint of the chemical evolution in galaxies has affected the distribution of H II regions across the most widely used diagnostic diagram, the so-called BPT diagram (e.g., Fig. 1). In this Appendix we show that this imprint not only affects the location within the BPT diagram. Indeed, in basically all the explored diagnostic diagrams, we find clear trends related to the properties of the underlying stellar population. Figure A.1 shows four additional diagnostic diagrams, different than the BPT diagram, built based on the comparison of the following emission line ratios: [O III] λ5007/Hβ, [N II] λ6583/Hβ, [O II] λ3727/Hβ, [S II] $\lambda\lambda$6717, 31/Hβ, and [O III] λ5007/[O II] λ3727. Each of these line ratios is more sensitive to different properties of the ionized gas and the ionizing sources. It is beyond the scope of this study to describe the particular dependencies of each one in detail, but they have been widely described in the literature (e.g., Veilleux & Osterbrock 1987; Dopita & Sutherland 1995; Cid Fernandes et al. 2010). However, regardless to which physical properties are more sensitive, Fig. A.1 shows that it is possible to identify trends in the luminosity-weighted age of the underlying stellar population in the four diagrams. In some cases the trend is stronger for one of the explored line ratios; e.g., in the [O III] λ5007/Hβ vs. [S II] $\lambda\lambda$6717, 31/Hβ diagram, the stellar age is more clearly associated with the first of the two parameters, while in the [O III] λ5007/[O II] λ3727 vs. [N II] λ6583/Hβ diagram, it is more clearly related to the second one. However, even in the case of the diagnostic diagram comparing the two line ratios with the apparent weaker dependence with the age of the stellar population ([O III] λ5007/[O II] λ3727 vs. [S II] λ6717, 31/Hβ), there are clear trends that depend on the two parameters at the same time.

In summary, we have shown that the main conclusion of the current study, i.e., that there is a tight relation between the properties of the H II regions and those of the underlying stellar population, is independent of the diagnostic diagram selected to explore this depedence.

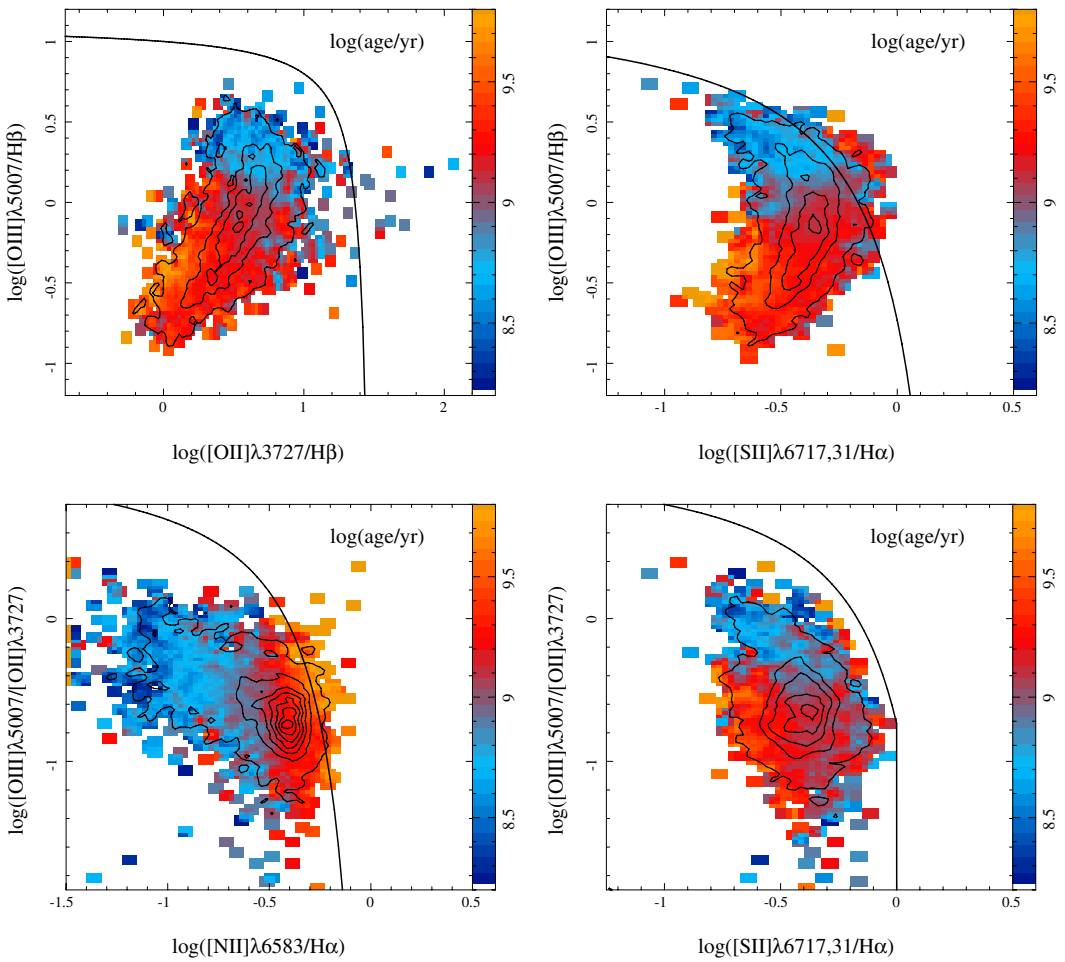

Fig. A.1. Distribution of the ~5000 H II regions included in our sample across four classical diagnostic diagrams: *top left panel,* [O III] λ5007/Hβ vs. [O II] λ3727/Hβ; *top right panel,* [O III] λ5007/Hβ vs. [S II] λ6717, 31/Hβ; *bottom left panel*, [O III] λ5007/[O II] λ3727 vs. [N II] λ6583/Hβ and *bottom right panel*, [O III] λ5007/[O II] λ3727 vs. [S II] λ6717, 31/Hβ. In each panel, the contours show the density distribution of the H II regions within considered diagram, with the outermost contour enclosing 95% of the regions, and each consecutive one enclosing 20% less regions. The color indicates the average luminosity weighted age of the underlying stellar population at the corresponding location in the diagram. The solid line represent the classical demarcation line used to select H II regions.